Normalized Convective Characteristics of Tropical Cyclone Rapid Intensification Events in the North Atlantic and Eastern North Pacific

MICHAEL S. FISCHER, BRIAN H. TANG, AND KRISTEN L. CORBOSIERO

Department of Atmospheric and Environmental Sciences, University at Albany, State University of New York, Albany, New York

CHRISTOPHER M. ROZOFF

National Center for Atmospheric Research, Boulder, Colorado

(Manuscript received 18 August 2017, in final form 26 February 2018)

ABSTRACT

The relationship between tropical cyclone (TC) convective characteristics and TC intensity change is explored using infrared and passive microwave satellite imagery of TCs in the North Atlantic and eastern North Pacific basins from 1989 to 2016. TC intensity change episodes were placed into one of four groups: rapid intensification (RI), slow intensification (SI), neutral (N), and weakening (W). To account for differences in the distributions of TC intensity among the intensity change groups, a normalization technique is introduced, which allows for the analysis of anomalous TC convective characteristics and their relationship to TC intensity change.

A composite analysis of normalized convective parameters shows anomalously cold infrared and 85-GHz brightness temperatures, as well as anomalously warm 37-GHz brightness temperatures, in the upshear quadrants of the TC are associated with increased rates of TC intensification, including RI. For RI episodes in the North Atlantic basin, an increase in anomalous liquid hydrometeor content precedes anomalous ice hydrometeor content by approximately 12 h, suggesting convection deep enough to produce robust ice scattering is a symptom of, rather than a precursor to, RI. In the eastern North Pacific basin, the amount of anomalous liquid and ice hydrometeors increases in tandem near the onset of RI.

Normalized infrared and passive microwave brightness temperatures can be utilized to skillfully predict episodes of RI, as the forecast skill of RI episodes using solely normalized convective parameters is comparable to the forecast skill of RI episodes by current operational statistical models.

1. Introduction

Improving tropical cyclone (TC) intensity forecasts is an important, but difficult problem. Despite recent improvements in TC intensity forecast skill, large improvements are still possible (DeMaria et al. 2014; Emanuel and Zhang 2016). Forecast error is particularly large for those TCs that rapidly intensify (Sampson et al. 2011; Emanuel and Zhang 2016). Although operational statistical and dynamical models display some skill in the prediction of rapid intensification (RI), the probability of detection of such episodes is low, while the false alarm rate is undesirably high (Kaplan et al. 2010; Rozoff and Kossin 2011; Kaplan et al. 2015; Rozoff et al. 2015). Consequently, the National Hurricane Center has prioritized improving the predictability of RI (Rappaport et al. 2012).

It is well known that RI, commonly defined as TC intensity change episodes that meet, or exceed, the 95th percentile of all overwater 24-h TC intensity changes (Kaplan and DeMaria 2003; Kaplan et al. 2010), occurs preferentially in favorable environments. Namely, RI is more likely to occur in environments characterized by, among other things, low vertical wind shear, high tropospheric humidity and oceanic heat content, and large upper-tropospheric divergence (Kaplan and DeMaria 2003; Kaplan et al. 2010; Rozoff and Kossin 2011; Tang and Emanuel 2012; Kaplan et al. 2015; Rozoff et al. 2015). These characteristics are, however, largely similar to the environmental characteristics of TCs that slowly intensify, suggesting that a favorable environment alone is insufficient for a TC to undergo RI and that convective-scale processes play an important role in RI (Hendricks et al. 2010; Tao and Jiang 2015; Tao et al. 2017). Indeed, incorporating the convective characteristics of TCs into statistical model predictions of RI adds skill to forecasts (Kaplan et al. 2010, 2015; Rozoff et al. 2015).

Corresponding author: Michael S. Fischer, msfischer@albany.edu

DOI: 10.1175/MWR-D-17-0239.1

Many studies have demonstrated robust differences between the convective characteristics of RI events and TCs that intensify at lesser rates. One of these differences is the presence of convective bursts, which are localized regions of robust updrafts with intense diabatic heating. RI case studies using both in situ and remote sensing observations (Guimond et al. 2010, 2016), as well as numerical modeling simulations (Zhang and Chen 2012; Chen and Zhang 2013; Wang and Wang 2014) have argued compensating subsidence, associated with convective bursts, acts to warm the TC core, resulting in RI. Other studies have emphasized the significance of the radial location of convective bursts (e.g., Rogers et al. 2013, 2015; Stevenson et al. 2018), as numerical modeling studies have shown that diabatic heating located inside the radius of maximum wind efficiently spins up the TC vortex (Schubert and Hack 1982; Shapiro and Willoughby 1982; Hack and Schubert 1986; Pendergrass and Willoughby 2009; Vigh and Schubert 2009). The azimuthal location of convective bursts may also be important in the alignment of tilted TC vortices in vertical wind shear, as seen in the RI of Hurricane Earl (2010; Stevenson et al. 2014; Rogers et al. 2015; Susca-Lopata et al. 2015).

Despite the linkages between convective bursts, which tend to be highly asymmetric features, and RI, numerical modeling simulations have demonstrated that a symmetric distribution of diabatic heating is a more efficient configuration for vortex intensification (Nolan and Grasso 2003; Nolan et al. 2007). Case studies of RI events performed by Kieper and Jiang (2012) noted that the presence of a convective ring feature in 37-GHz passive microwave imagery was frequently a harbinger of RI. Since 37-GHz passive microwave imagery is sensitive to emission from liquid hydrometeors (Wu and Weinman 1984; Lee et al. 2002), Kieper and Jiang (2012) argued for the importance of symmetric rings of warm rain in the initiation of RI. The significance of symmetric convection in RI was also advocated in subsequent studies by Zagrodnik and Jiang (2014) and Tao and Jiang (2015), who used passive microwave imagery to composite the convective characteristics of multiple intensity change groups, ranging from weakening TCs to those that rapidly intensify. The composites of RI episodes in these analyses consistently displayed greater azimuthal coverage of convection, especially shallow convection, than composites of TCs that intensify at lesser rates. Other studies, however, that used passive microwave imagery to composite TC intensity change events have emphasized the link between the presence of ice hydrometeors, either from stratiform precipitation or convection that penetrates above the freezing level, and RI (Harnos and Nesbitt 2011; Alvey et al. 2015; Harnos and Nesbitt 2016a). These studies used passive microwave frequencies sensitive to ice scattering (e.g., 85–91 GHz) to demonstrate how RI episodes are associated with more symmetric convection, which can include the presence of convective ring features containing ice and mixed phase microphysical processes (Harnos and Nesbitt 2011, 2016a). Similarly, Kaplan et al. (2015) also determined RI episodes are associated with more symmetric convection through an analysis of TC infrared brightness temperatures.

The role of stratiform precipitation versus deep convection in RI may depend on how an RI *event* is treated. As noted by Tao et al. (2017), an individual RI event can be composed of several consecutive 24-h RI *episodes*. In fact, the majority of RI events last longer than the commonly used 24-h criterion for RI episodes (Tao et al. 2017). Consequently, previous studies have separated RI events into initial RI episodes (e.g., RI episodes in the first 12 h of an RI event) and continuing RI episodes, defined as RI episodes beginning at least 12 h after the onset of an RI event (Zagrodnik and Jiang 2014; Tao and Jiang 2015; Tao et al. 2017). When this distinction is made, prior work has discovered an increase in convective ascent occurring below, or near, the freezing level and stratiform precipitation appears to play an important role in the initiation of RI, whereas an increase in deep convection tends to be a symptom of RI itself, rather than the trigger of RI (Zagrodnik and Jiang 2014; Tao and Jiang 2015; Tao et al. 2017).

Interestingly, recent numerical modeling simulations of two RI events analyzed by Harnos and Nesbitt (2016b, c) suggest that the relationship between the symmetry and vigor of convection in RI is also dependent upon the magnitude of the vertical wind shear. A simulated RI event in relatively weak vertical wind shear was characterized by symmetric stratiform precipitation near the onset of RI, while a separate simulated RI event occurring in an environment characterized by stronger vertical wind shear displayed more asymmetric and vigorous convection (Harnos and Nesbitt 2016b, c). These simulations are also consistent with the composite analysis of Harnos and Nesbitt (2011), which found RI episodes in relatively strong vertical wind shear tended to have more robust ice scattering.

An additional complication is that prior work grouped TCs across a spectrum of initial intensities to compare the composite structure of TCs that underwent RI versus those that did not. Since TCs generally have more organized convective structures as TC intensity increases (Dvorak 1975; Cecil and Zipser 1999; Velden et al. 2006), differences in the composite convective characteristics between TC intensity change groups may be due to differences in the mean initial intensities between the intensity change groups. For example, previous analyses

have found TCs that weaken tend to have greater initial intensities than TCs that strengthen (Tang and Emanuel 2012; Zagrodnik and Jiang 2014; Alvey et al. 2015; Tao and Jiang 2015; Tao et al. 2017). Conversely, TCs that undergo RI tend to have significantly larger initial intensities than slowly intensifying TCs (Tao and Jiang 2015; Tao et al. 2017). As a result, it is unclear to what extent the conclusions drawn from the composite convective differences between intensity change groups in prior studies stem from differing initial intensities.

To gain additional insight into the convective characteristics of RI episodes, we introduce a novel convective normalization technique, which accounts for variations in the convective structure of TCs caused by differences in initial TC intensity. By normalizing the convective structures of TCs based on initial TC intensity, the relationship between *anomalous* brightness temperatures and TC intensity change can be analyzed for TCs across all intensities. Thus, the ultimate goal of this paper is to clarify the relationships between the anomalous convective characteristics of TCs and TC intensity change, including RI. For the purpose of this analysis, ''convection'' will refer to any type of moist, vertical, or slantwise, overturning motion associated with hydrometeors, including both stratiform precipitation and tropospheric-deep cumulonimbus towers, as diagnosed by infrared and passive microwave satellite imagery.

In section 2, we describe the datasets and methods employed in this analysis. The observed convective characteristics of the TCs examined in this study are discussed in section 3. Section 4 introduces the convective normalization technique and assesses the role of anomalous convective activity in TC intensity change. Section 5 explores how anomalous convective activity is related to RI onset. Section 6 demonstrates how normalized convective characteristics can be used to skillfully predict RI. A discussion and summary of the findings of this paper are presented in section 7.

2. Data and methods

a. Datasets

This study analyzes tropical and subtropical cyclones forming in the North Atlantic and eastern North Pacific basins during 1989–2016. Storm intensities and position estimates are taken from the National Hurricane Center (NHC) ''best track'' hurricane database (HURDAT2; Landsea and Franklin 2013). This study only focuses on the overwater portion of a given TC's life cycle. Additionally, TCs that were located in environments characterized by a maximum potential intensity $< 40\,\mathrm{m\,s^{-1}}$ were removed from this dataset. This criterion eliminates TCs unlikely to intensify because of unfavorable thermodynamic environmental conditions, such as those over relatively cold sea surface temperatures, and also acts to filter out those TCs more likely to undergo extratropical transition (Hart and Evans 2001). The environmental maximum potential intensity was calculated following Bister and Emanuel (2002) with fields from the European Centre for Medium-Range Weather Forecasts interim reanalysis (ERA-Interim; Dee et al. 2011). Data from the ERA-Interim are available four times daily with a horizontal resolution of approximately $0.7° \times 0.7°$.

A portion of the TC convective analysis in this study uses infrared (IR) brightness temperatures retrieved from the GridSat dataset (Knapp et al. 2011). IR brightness temperatures from the GridSat dataset are available eight times daily at a spatial resolution of approximately 10 km. Using IR brightness temperatures to diagnose the convective characteristics of TCs has the benefit of consistent temporal and spatial sampling at the cost of the observations being limited to sampling the structure of cloud tops.

The remainder of the convective analysis utilizes passive microwave satellite imagery from low-Earth-orbiting satellites, which have the ability to detect liquid or frozen hydrometeors underneath the cirrus canopy. Because of the nature of the low-Earth orbit of the microwave satellites, however, the sampling of a given TC can be temporally inconsistent as a result of instances where the scanning swath of the satellite either partially, or completely, misses the TC. This study utilizes microwave brightness temperatures observed from six low-Earth-orbiting satellites: the Advanced Microwave Scanning Radiometer for Earth Observing System (AMSR-E), the Advanced Microwave Scanning Radiometer 2 (AMSR-2), the Special Sensor Microwave Imager (SSM/I), the Special Sensor Microwave Imager/Sounder (SSMIS), the Tropical Rainfall Measuring Mission Microwave Imager (TMI), and the Global Precipitation Measurement mission Microwave Imager (GMI). The microwave frequencies used in this analysis, and their corresponding spatial footprints, are shown in Table 1. For each frequency shown in Table 1, horizontally polarized, vertically polarized, and polarization-corrected brightness temperatures (PCT) were analyzed.

For simplicity, this study will solely use 37-GHz horizontally polarized brightness temperatures and 85-GHz PCT, as these two spectral channels were found to have the strongest correlations to future TC intensity change from their respective frequencies (not shown). The 37-GHz channel is sensitive to emissions from an increased liquid water path (e.g., Wu and Weinman 1984; Spencer et al. 1989) and, as a result, is primarily a representation of precipitation below the freezing level,

TABLE 1. Frequencies and footprints for each of the passive microwave sensors used in this analysis.

	Low-frequency channel		High-frequency channel	
Sensor	Frequency (GHz)	Footprint (km×km)	Frequency (GHz)	Footprint (km×km)
SSM/I	37.0	37 × 28	85.5	15 × 13
SSMIS	36.5	45 × 31	91.655	16 × 13
TMI	37.0	18 × 10	85.5	8 × 6
GMI	36.5	15 × 9	89.0	7 × 4
AMSR-E	36.5	14 × 8	89.0	6 × 4
AMSR-2	36.5	12 × 7	89.0	5 × 3

with warmer brightness temperatures indicative of increased liquid hydrometeor content from either shallow convection or deep convection without appreciable ice water path. A caveat to this interpretation is that 37-GHz brightness temperatures can also be enhanced in regions without appreciable liquid hydrometeor content because of a disturbed sea state via increased surface wind speeds, as demonstrated by Harnos and Nesbitt (2016a). Signatures detected in the 85-GHz channel, especially 85-GHz PCT < 250 K, are mainly due to scattering by ice water path above the freezing level mainly by larger hydrometeors, such as hail and graupel (e.g., Wilheit 1986; Vivekanandan et al. 1991; Harnos and Nesbitt 2016a).

Data from the microwave overpasses were processed onto TC-centered polar grids, using the objective TC center finding algorithm of Wimmers and Velden (2010), known as the Automated Rotation Center Hurricane Eye Retrieval (ARCHER). Because of potential parallax issues associated with the 37- and 85-GHz channels employed in this analysis, TCs were centered using horizontally polarized brightness temperatures for both frequencies, as in Rozoff et al. (2015). As seen in Table 1, differences exist between the low- and high-frequency channels of the six microwave sensors used in this analysis. Although the physical interpretations of both the low- and high-frequency channels are similar, despite the small differences in frequency between the respective channels, observed brightness temperatures can vary by as much as 10 K between sensors (Jones and Cecil 2006; Hawkins et al. 2008). To account for these differences, brightness temperatures in all spectral channels were calibrated using a histogram matching technique, similar to Jones and Cecil (2006) and Rozoff et al. (2015). Specifically, observations from the SSM/I, SSMIS, TMI, and AMSR-E were calibrated to observations from the AMSR-2 and GMI. Using the calibrated brightness temperatures, overpasses were paired with all available best track TC entries that occurred within 3 h of the overpass. If multiple overpasses could be paired with a given best track entry, the sensor with the greatest spatial resolution was selected. Since brightness temperatures of land surfaces in clear conditions can be of similar magnitudes to intense precipitation, any grid points that were observed overland were replaced with missing values.

b. *Intensity change groups and compositing methodology*

This study analyzes TC intensity change episodes based on the following 24-h change in maximum sustained 10-m wind speed (ΔV_{max}). Based on the magnitude of ΔV_{max}, TC intensity change episodes in the North Atlantic and eastern North Pacific basins are placed into one of four groups: rapid intensification (RI), slow intensification (SI), neutral (N), and weakening (W). The criterion used for the intensity change groups and the corresponding number of cases are provided in Table 2. Note that unless specified otherwise, RI episodes refer to any TC that meets the criterion for RI, regardless of when the episode occurs within the encompassing RI event. Section 5 of this analysis will discuss how the characteristics of RI can vary with time.

For reference, the distributions of all TC intensity change episodes that meet the aforementioned criteria for the North Atlantic and eastern North Pacific basins are shown in Fig. 1. The eastern North Pacific basin is

TABLE 2. Intensity change definitions and corresponding number of episodes for the North Atlantic (ATL) and eastern North Pacific (EPAC) basins. Note ΔV_{max} represents the 24-h change in maximum sustained 10-m winds.

Intensity change group	ATL criterion	ATL episode total	EPAC criterion	EPAC episode total
Rapid intensification (RI)	$\Delta V_{max} \geq 30$ kt	374	$\Delta V_{max} \geq 35$ kt	453
Slow intensification (SI)	$30 > \Delta V_{max} > 10$ kt	1270	$35 > \Delta V_{max} > 10$ kt	1729
Neutral (N)	$10 \geq \Delta V_{max} \geq -10$ kt	3718	$10 \geq \Delta V_{max} \geq -10$ kt	3647
Weakening (W)	$\Delta V_{max} < -10$ kt	649	$\Delta V_{max} < -10$ kt	1433

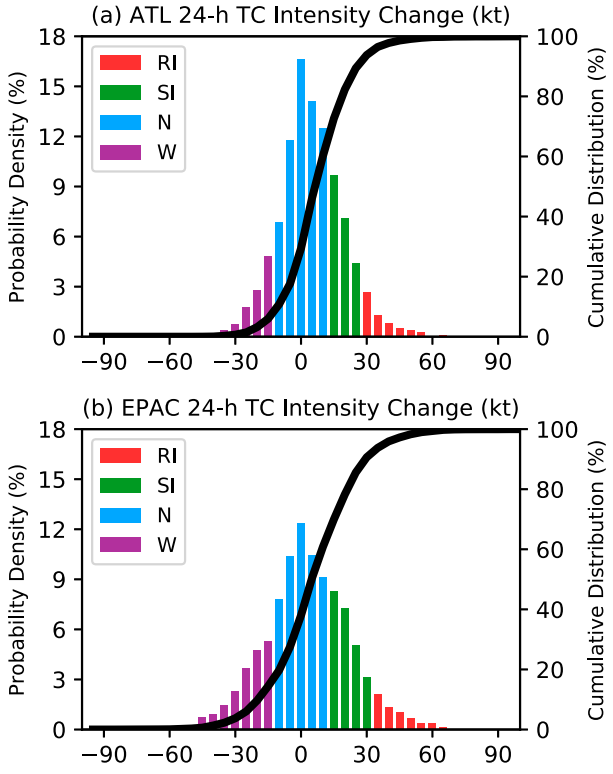

FIG. 1. 24-h intensity change distribution of all overwater TCs occurring during 1989–2016 in environments characterized by a maximum potential intensity of at least 40 m s^{-1} for the (a) North Atlantic and (b) eastern North Pacific basins. The probability density (%) is given by the bars, with RI episodes colored in red, SI episodes in green, N episodes in blue, and W episodes in purple. The cumulative distribution (%) is represented by the black line.

associated with TC intensity change episodes that are more normally distributed, which is consistent with the findings of Kaplan et al. (2010). For both basins, RI episodes were determined to be in the 95th percentile of ΔV_{max}. Since the eastern North Pacific basin features intensity change episodes with larger tails in the distribution, the ΔV_{max} threshold for RI episodes in the eastern North Pacific is 35 kt (1 kt = 0.5144 m s^{-1}), which is higher than the 30-kt threshold for the North Atlantic basin.

Storm-centered composites of the four intensity change groups are frequently utilized in this analysis. Composites are rotated with respect to the direction of the vertical wind shear, as previous studies have demonstrated vertical wind shear acts as an important modulator of the convective structure of TCs (Corbosiero and Molinari 2002, 2003; Chen et al. 2006; DeHart et al. 2014). For the purposes of this study, the vertical wind shear is calculated between 1000 and 250 hPa, using the Davis et al. (2008) TC vorticity inversion technique to filter out the TC's winds before calculating the shear. A radius of 400 km was used for the inversion technique. The pressure levels chosen were found to have the strongest correlation to future 24-h TC intensity change after testing a variety of deep-layer shear heights and TC vorticity inversion radii (not shown).

3. Convective characteristics of tropical cyclone intensity change episodes

a. *Infrared brightness temperatures*

Storm-centered, shear-relative, composite-mean IR brightness temperatures for the four intensity change groups in both the North Atlantic and eastern North Pacific basins are shown in Fig. 2. For reference, the number of TCs included in each composite is listed in Table 3. The composites of RI, SI, and N episodes in the eastern North Pacific basin are associated with colder IR brightness temperatures than the corresponding intensity change group composites in the North Atlantic basin (Figs. 2a–c and 2e–g). Additionally, with the exception of eastern North Pacific RI episodes, the coldest IR brightness temperatures are displaced downshear of the TC center (Figs. 2a–d and 2f–h), which is consistent with previous work (Corbosiero and Molinari 2002, 2003; Chen et al. 2006; DeHart et al. 2014). For each intensity change group, TCs in the North Atlantic basin tend to be more asymmetric, having a greater downshear displacement of the location of minimum IR brightness temperatures, than TCs in the eastern North Pacific. Additionally, TCs in the North Atlantic tend to have a greater upshear radial gradient of IR brightness temperatures than TCs in the eastern North Pacific basin. These results may be partially attributed to the fact that, with the exception of RI episodes, each intensity change group in the North Atlantic is associated with larger vertical wind shear magnitudes than the corresponding intensity change group in the eastern North Pacific (Table 4).

In both basins, the composites of RI episodes display the coldest and most symmetric IR brightness temperatures of their respective basins (Figs. 2a and 2e). As the rate of intensification decreases, the pattern of IR brightness temperatures becomes increasingly asymmetric and the composite-minimum IR brightness temperatures warm, with the exception of W episodes. In fact, W episodes are associated with IR brightness temperatures colder than N and SI episodes in the North Atlantic basin (Figs. 2b–d) and the N episodes in the eastern North Pacific basin (Figs. 2g,h). This result suggests that cold IR brightness temperatures can be associated with both RI and W episodes. Furthermore, W episodes are the only composites to display an eye feature, denoted by a local maximum in IR brightness

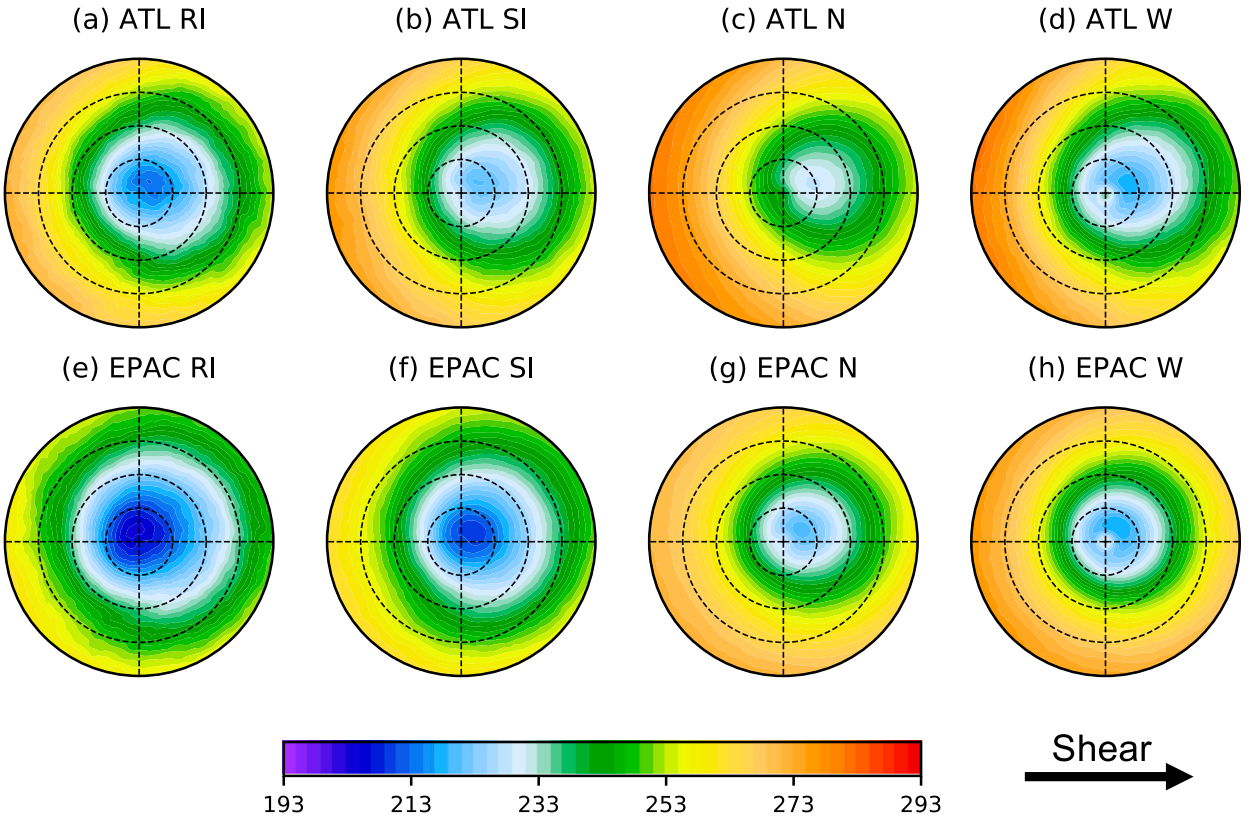

FIG. 2. Composite-mean, storm-centered, shear-relative, IR brightness temperatures (K) for (a) RI, (b) SI, (c) N, and (d) W episodes in the North Atlantic basin. Composites are shown at the beginning of the 24-h intensity change episode. Each composite is rotated by the deep-layer (1000–250 hPa) environmental vertical wind shear direction, with the shear vector pointing to the right side of each panel, as denoted by the black vector. Dashed radial rings are spaced in 100-km increments. (e)–(h) As in (a)–(d), but for TCs in the eastern North Pacific basin.

temperature at the TC center, surrounded by a ring of colder IR brightness temperatures (Figs. 2d and 2h).

b. Microwave brightness temperatures

Figure 3 shows storm-centered, shear-relative, composite-mean 37-GHz horizontally polarized brightness temperatures. Note that the microwave brightness temperatures in Fig. 3 are shown for the innermost 200 km, instead of the innermost 400 km as in Fig. 2, and the sample size of episodes comprising the microwave composites is smaller than the sample size of episodes comprising the IR brightness composites (Table 3). Recall the 37-GHz channel is primarily a representation of liquid hydrometeor content, with warmer brightness temperatures indicative of increased liquid water path from either shallow convection or deep convection without appreciable ice content. In each composite, the maximum 37-GHz brightness temperatures are found in the downshear-left quadrant. For each intensity change group, composites in the eastern North Pacific basin display warmer maximum 37-GHz brightness temperatures than the corresponding North Atlantic composites. The location of the warmest 37-GHz brightness temperatures in the eastern North Pacific composites is

TABLE 3. Number of intensity change episodes with available infrared (IR) and passive microwave (MW) imagery for the North Atlantic (ATL) and eastern North Pacific (EPAC) basins.

Intensity change group	ATL IR	ATL MW	EPAC IR	EPAC MW
Rapid intensification (RI)	370	217	438	205
Slow intensification (SI)	1257	715	1667	763
Neutral (N)	3692	1942	3480	1510
Weakening (W)	645	370	1366	654

TABLE 4. Mean deep-layer (1000–250 hPa) vertical wind shear ($m\,s^{-1}$) for rapid intensification (RI), slow intensification (SI), neutral (N), and weakening (W) episodes in the North Atlantic (ATL) and eastern North Pacific (EPAC) basins.

Basin	RI	SI	N	W
ATL	5.0	6.1	7.9	9.4
EPAC	5.3	5.9	6.2	5.9

more cyclonically downwind than the corresponding North Atlantic composites. This difference may be the result of both lighter vertical wind shear magnitudes in the eastern North Pacific, with the exception of RI episodes (Table 4), as well as a different distribution of shear directions relative to the TC motion vector (e.g., Chen et al. 2006; Stevenson et al. 2016). North Atlantic composites are also associated with a greater upshear radial gradient of 37-GHz brightness temperatures than the respective eastern North Pacific composites.

Similar to Fig. 2, the 37-GHz composites of RI episodes display the most symmetric convection in their respective basins (Figs. 3a and 3e). The RI composites also feature a closed ring of enhanced 37-GHz brightness temperatures around the TC center, consistent with the 37-GHz composites of Tao and Jiang (2015) and Harnos and Nesbitt (2016a). In both basins, the composite convective structure becomes less organized, with brightness temperatures cooling and the convective pattern becoming increasingly asymmetric, going from the RI to SI to N episodes (Figs. 3a–c and 3e–g). The W episodes (Figs. 3d and 3h) are associated with maximum 37-GHz brightness temperatures and the most distinct eye out of any of the intensity change groups. These patterns again suggest that maximum 37-GHz brightness temperatures cannot distinguish between intensity change groups by itself.

The relationship between composited 85-GHz brightness temperatures and future TC intensity change is relatively similar to Fig. 3, with RI episodes associated with more symmetric convection about the TC center (not shown).

4. Normalized convective characteristics of tropical cyclone intensity change episodes

a. *Influence of tropical cyclone initial intensity*

Figure 4 shows that the distributions of TC intensity that compose the four intensity change groups differ markedly. In both basins, W episodes are associated

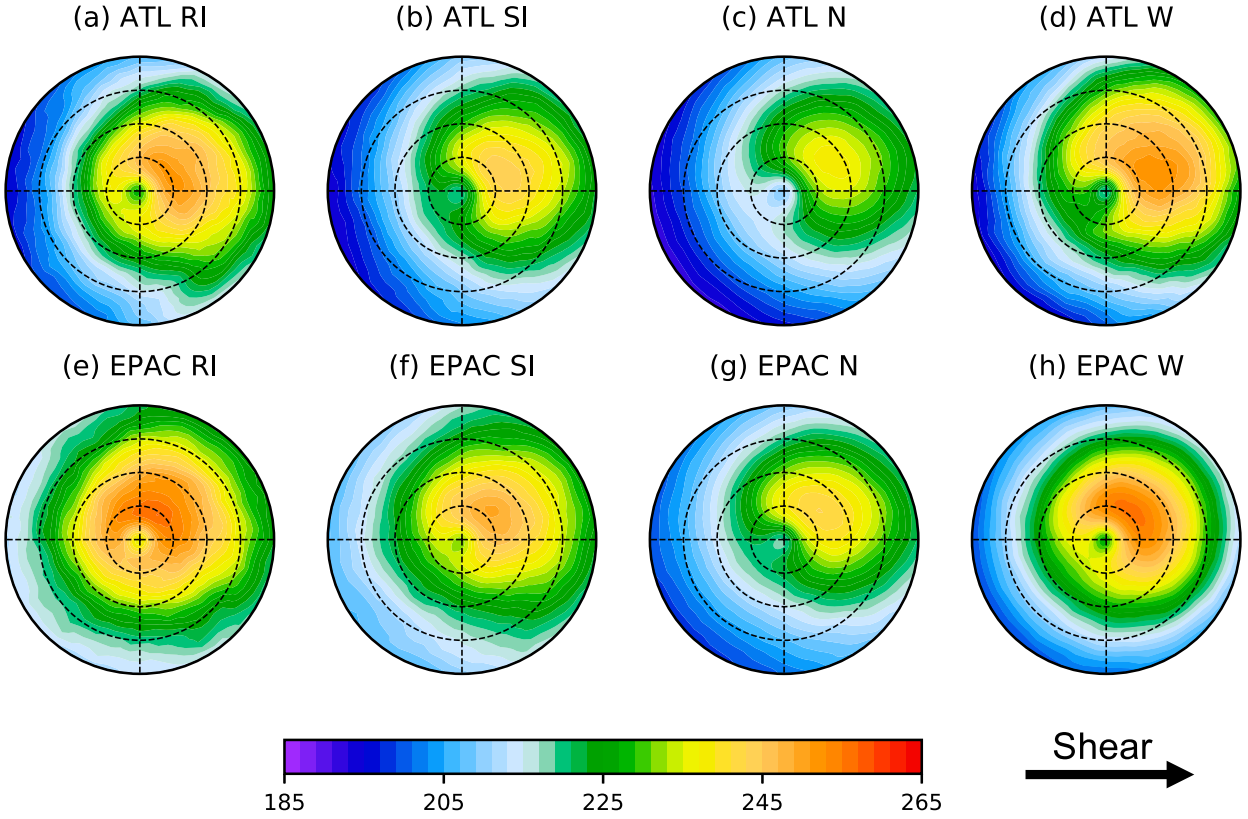

FIG. 3. As in Fig. 2, but for 37-GHz horizontally polarized brightness temperatures (K). Dashed radial rings are spaced in 50-km increments.

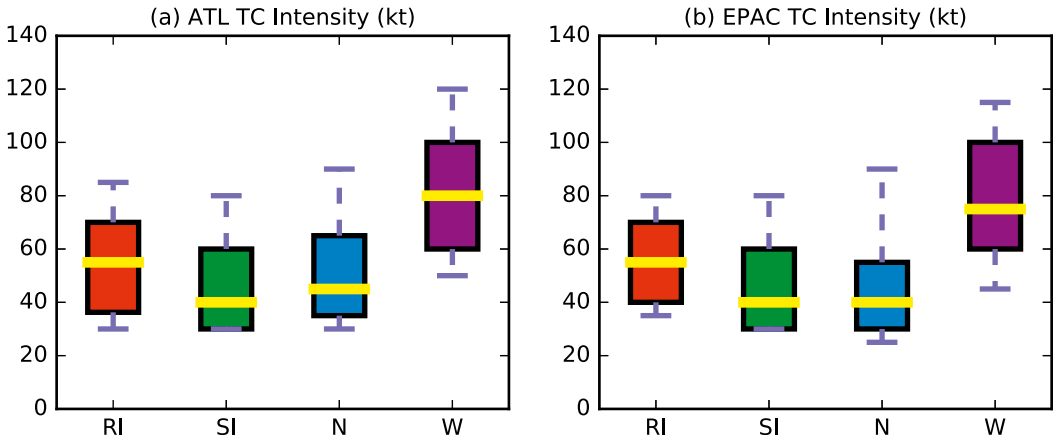

FIG. 4. Box-and-whisker plots of TC intensity (kt) at the onset of the intensity change episode, separated by TC intensity change group, for available IR observations in the (a) North Atlantic basin and (b) eastern North Pacific basin. The colored boxes denote the 25th–75th percentiles, with a yellow line at the median. The horizontal dashed lines (whiskers) extend to the 10th and 90th percentiles.

with the strongest TCs of the four intensity change groups. In fact, the intensity distribution of W episodes is statistically significantly stronger compared to the intensity distributions of the other intensity change groups using the nonparametric, two-tailed Wilcoxon rank sum test (Wilks 2011). Hereafter, any mention of statistical significance will be in reference to a confidence level of at least 95% using this test. Additionally, the intensity distribution of RI episodes is significantly stronger than the intensity distributions of both SI and N episodes.

Previous work has demonstrated that TC convective organization increases as TC intensity increases. Stronger TCs feature greater convective organization on IR satellite imagery (Dvorak 1975; Velden et al. 2006, 2017) and are associated with warmer (colder) brightness temperatures in 37-GHz (85 GHz) passive microwave imagery (Cecil and Zipser 1999). As a result, the greater initial intensity of W episodes likely explains why W episodes display greater convective activity than N and SI episodes in the passive microwave composites (Fig. 3), and display a distinct eye in IR composites (Fig. 2). A similar argument can be made for RI episodes, which are also more intense, and associated with more intense and organized convection, than SI and N episodes. To clarify the relationship between TC intensity change and TC convective organization, differences in the distributions of TC intensity need to be taken into account.

b. *Normalization technique methodology*

To account for differences in intensity distributions between the intensity change groups, we normalize the IR and microwave brightness temperatures using the following procedure, which is analogous to the calculation of a z score:

$$T_b^* = \frac{T_b - \overline{T_b}}{\sigma}, \tag{1}$$

where T_b^* is the normalized brightness temperature, T_b is the observed brightness temperature, $\overline{T_b}$ is the mean of the climatological brightness temperature, and σ is the standard deviation of the climatological brightness temperature. For each TC, the brightness temperature fields are rotated such that the shear vector is in the same direction. The calculation of the climatological brightness temperatures was performed by first identifying all TCs within ±5 kt of a given TC intensity. The ±5-kt range is within the range of uncertainty of typical TC intensity estimates (e.g., Torn and Snyder 2012; Landsea and Franklin 2013) and increased the sample size for each calculation of $\overline{T_b}$. Since there are more TCs with lower initial intensities, however, those TCs falling within the ±5-kt interval were randomly selected to prevent the climatology from being biased toward the convective structure of the more frequent intensities. For example, for the calculation of the climatology of 100-kt TCs, all TCs with an intensity between 95 and 105 kt were identified. Hypothetically, if there existed 120 cases with an intensity of 95 kt, 110 cases with an intensity of 100 kt, and 90 cases with an intensity of 105 kt, 90 TCs were randomly selected, with replacement, from the 95-, 100-, and 105-kt samples. Then, the mean and standard deviation of the randomly sampled TCs were calculated. The random sampling process was repeated for a total of 50 iterations, and the mean of all 50 iterations was then used for the final climatological values. This process was carried out for TC intensities ranging from 30 to 135 kt. For TCs with an initial intensity greater than 135 kt, the calculation of climatological brightness temperatures used all TCs with

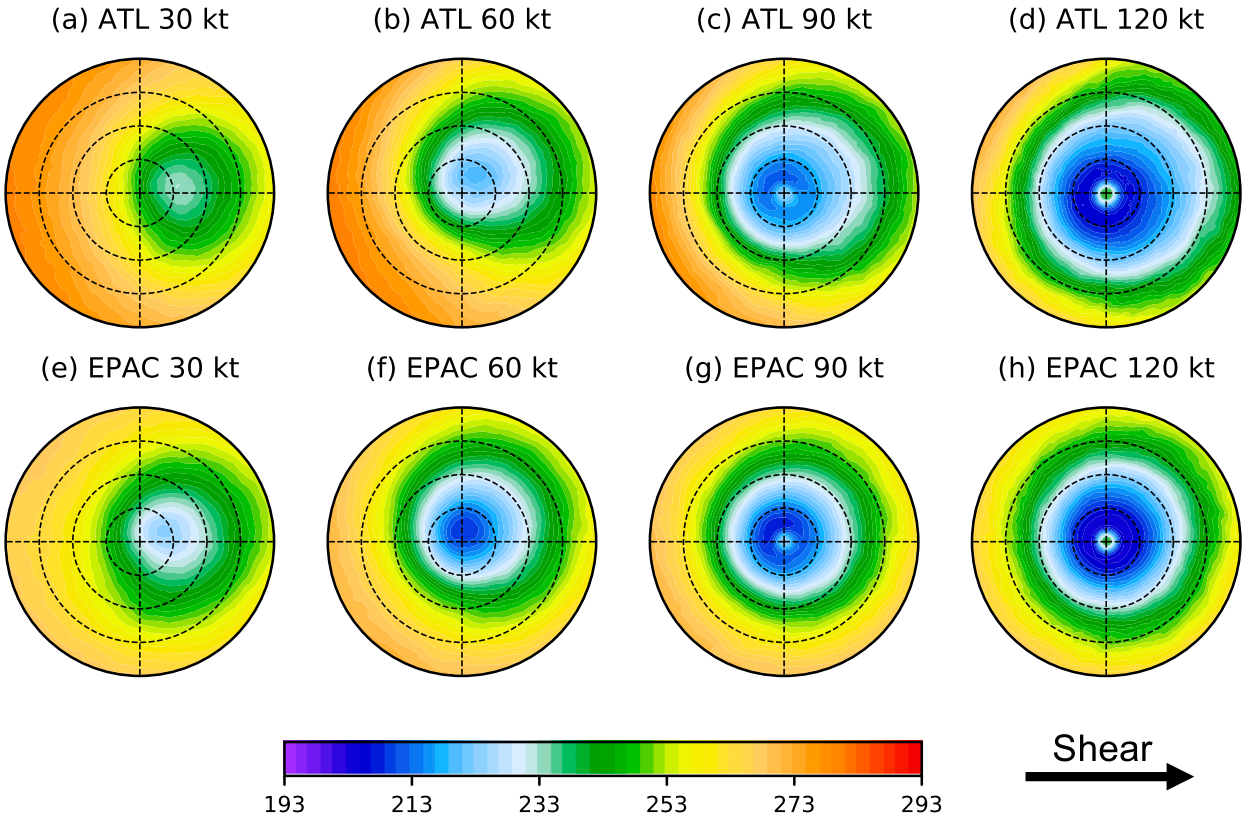

FIG. 5. Composite-mean, storm-centered, shear-relative, infrared brightness temperatures (K) for all TCs with intensities within ±5 kt of (a) 30, (b) 60, (c) 90, and (d) 120 kt in the North Atlantic basin. Each composite is rotated by the deep-layer (1000–250 hPa) environmental vertical wind shear direction, with the shear vector pointing to the right side of each panel, as denoted by the black vector. Dashed radial rings are spaced in 100-km increments. (e)–(h) As in (a)–(d), but for TCs in the eastern North Pacific basin.

intensities greater than 135 kt, because of the relatively small sample size.

Examples of the mean climatological IR brightness temperatures are shown in Fig. 5 for multiple TC intensities. As expected, as TC intensity increases, the climatological IR brightness temperatures display increased symmetry. Additionally, climatological IR brightness temperatures in the eastern North Pacific basin are consistently associated with colder brightness temperatures than the corresponding North Atlantic climatological composites. At 30 kt, convection is highly asymmetric and displays minimum brightness temperatures downshear of the TC center (Figs. 5a and 5e). As intensities exceed hurricane strength, an eye becomes increasingly apparent, surrounded by a ring of colder and more symmetric brightness temperatures (Figs. 5c,d and 5g,h). Climatological brightness temperatures from passive microwave brightness temperatures display a similar pattern (not shown).

After the climatological brightness temperatures were calculated, the brightness temperatures of all TCs within the dataset were normalized using Eq. (1). Two examples of the normalization process are provided in Fig. 6 for the cases of Hurricane Joaquin (2015) and Tropical Storm Fred (2009). Both of these TCs displayed asymmetric IR brightness temperatures, with convection focused primarily downshear of the TC center (Figs. 6a and 6e). The asymmetric convective pattern associated with Joaquin, however, differed greatly from the climatology of TCs of Joaquin's intensity of 105 kt, which are associated with a symmetric ring of convection about an eye (Figs. 6a,b). Furthermore, since there is typically relatively little variation in the brightness temperatures near the TC center for TCs of Joaquin's intensity, as denoted by the low climatological standard deviation outward of the eye region (Fig. 6c), the asymmetric convective pattern of Joaquin was quite anomalous for a TC of its intensity. The normalization demonstrates that Joaquin had IR brightness temperatures that were predominantly warmer over about three-quarters of its circulation than TCs of comparable intensity (Fig. 6d). Consistent with the anomalously warm IR brightness temperatures, the intensity of Hurricane Joaquin decreased by 30 kt in the following 24 h.

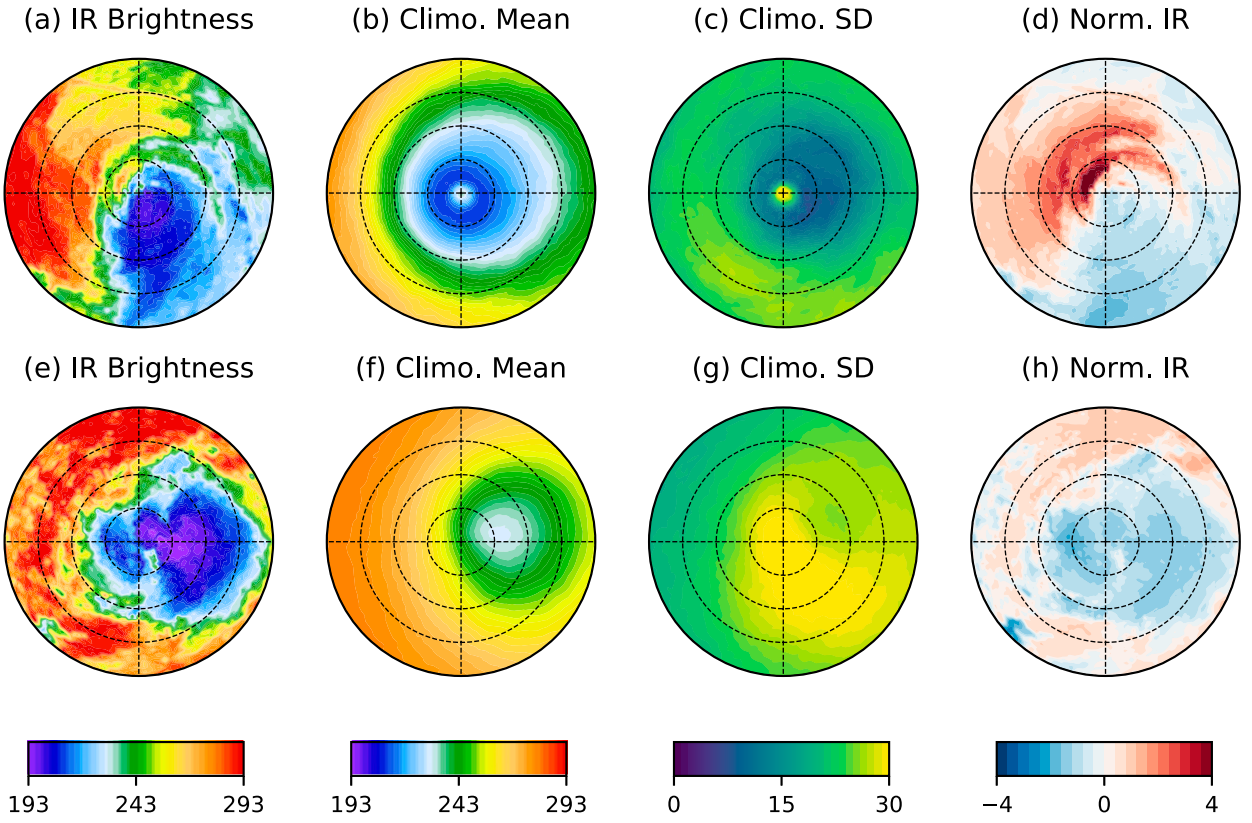

FIG. 6. (a) Storm-centered, shear-relative, infrared brightness temperatures for Hurricane Joaquin observed at 0600 UTC 4 Oct 2015. (b) Climatological mean infrared brightness temperatures (K) for all TCs in the North Atlantic basin with intensities within ±5 kt of Hurricane Joaquin (105 kt). (c) As in (b), but for the climatological standard deviation of infrared brightness temperatures (K). (d) Normalized infrared brightness temperatures resulting from subtracting the climatological mean values in (b) from the observed values in (a) and then dividing by the climatological standard deviation in (c). (e)–(h) As in (a)–(d), but for Tropical Storm Fred (35 kt) at 0000 UTC 8 Sep 2009. For each panel, the shear vector points toward the right side of the figure. Dashed radial rings are spaced in 100-km increments.

On the other hand, the convective pattern of Tropical Storm Fred was more organized than the typical TC with an intensity of 35 kt, with IR brightness temperatures colder than the climatological mean throughout almost all of the innermost 200 km (Figs. 6e,f). Although there exists a relatively large variation in the climatological IR brightness temperatures for TCs of Fred's intensity (Fig. 6g), the normalized IR brightness temperatures were negative throughout the innermost 200 km, indicating anomalously cold IR brightness temperatures (Fig. 6h). Correspondingly, Tropical Storm Fred underwent RI, intensifying by 35 kt in the following 24 h.

c. *Composite normalized convective characteristics*

The relationship between normalized IR brightness temperatures and the following 24-h TC intensity change in the two examples shown in Fig. 6 motivates the question of whether a similar relationship exists when the normalization is applied to all TCs in the dataset. To address this question, storm-centered, shear-relative composites of normalized IR and microwave brightness temperatures were created for the four intensity change groups. The composites of normalized IR brightness temperatures are shown in Fig. 7. In contrast to the raw IR composites in Fig. 2, the differences due to TC intensity have been accounted for through the normalization technique, resulting in a clear progression of increasing anomalously cold IR brightness temperatures (more negative values) going from W to RI episodes (right to left in Fig. 7). The range of normalized IR brightness temperatures among the intensity change groups is greater in the eastern North Pacific basin than the North Atlantic; however, the pattern of normalized brightness temperature progression between intensity change groups is similar.

In both basins, RI episodes are associated with the most negative composite normalized IR brightness temperatures, indicative of anomalously cold IR brightness temperatures (Figs. 7a and 7e). Interestingly, these negative anomalies are most pronounced in the upshear quadrants within approximately 200 km of the TC center, suggesting

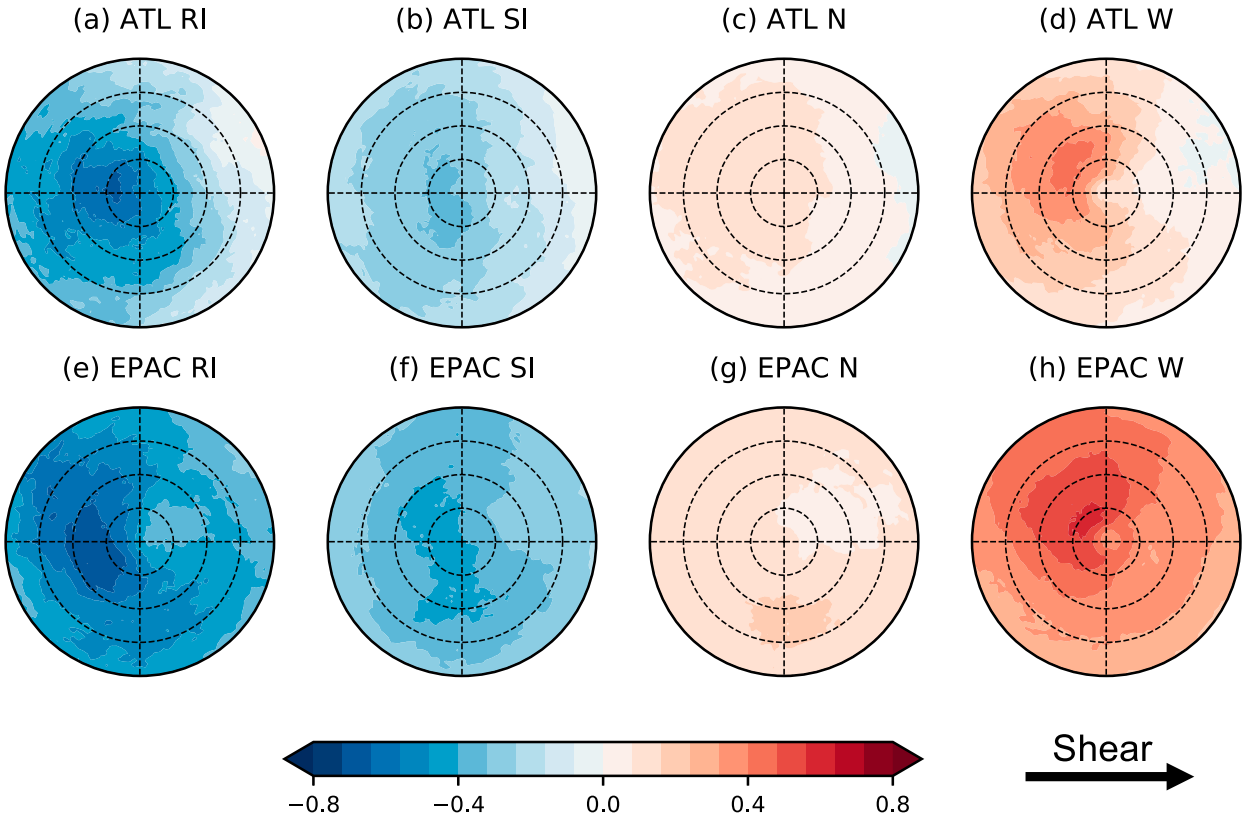

FIG. 7. As in Fig. 2, but for normalized infrared brightness temperatures. Regions of positive (negative) values are representative of anomalously warm (cold) IR brightness temperatures.

that anomalous upshear convection is associated with RI. The composites of SI episodes also feature negative normalized IR brightness temperatures, but the magnitudes of the negative anomalies are not as large as the RI composites (Figs. 7b and 7f). The composites of N episodes are characterized by anomalies of the weakest magnitudes, with anomalously warm IR brightness temperatures observed throughout nearly all of the innermost 400 km (Figs. 7c and 7g). Normalized IR brightness temperatures in W episodes display the strongest positive anomalies of the four intensity change groups, which are most pronounced in the upshear-left quadrant (Figs. 7d and 7h).

The normalization technique was also applied to microwave brightness temperatures. Figure 8 shows composites of normalized 37-GHz brightness temperatures for each of the intensity change groups. Recall warm 37-GHz brightness temperatures may indicate anomalously large liquid hydrometeor content. The composites of normalized 37-GHz brightness temperatures for RI episodes are again associated with the most anomalous convective activity upshear of the TC center (Figs. 8a and 8e), consistent with the more symmetric convection observed in Figs. 3a and 3e. The remaining intensity change groups follow a reverse progression as the normalized IR brightness temperatures in Fig. 7. For RI episodes in the North Atlantic, as well as W episodes in both basins, the locations of the most anomalous normalized 37-GHz brightness temperatures (Figs. 8a,d,h) are located cyclonically downwind of the most anomalous convection in IR imagery (Figs. 7a,d,h).

The normalized 85-GHz PCT, shown in Fig. 9, is consistent with the progression in Figs. 7 and 8, with RI episodes associated with the most negative normalized 85-GHz PCT, indicative of anomalously large ice hydrometeor content and, in turn, larger amounts of deep convection and/or stratiform precipitation resulting from deep convection (Figs. 9a and 9e). In both basins, for RI and SI episodes, the locations of the most anomalously negative 85-GHz PCT (Figs. 9a,b,e,f) are farther outward than the locations of the most anomalously positive 37-GHz brightness temperatures (Figs. 8a,b,e,f), perhaps because of the advection of ice hydrometeors by the radial outflow of the TC. As before, lesser intensification rates have anomalously weak convection, with the exception of W episodes in the North Atlantic, which display anomalously cold 85-GHz PCT throughout much of the downshear-left quadrant (Fig. 9d).

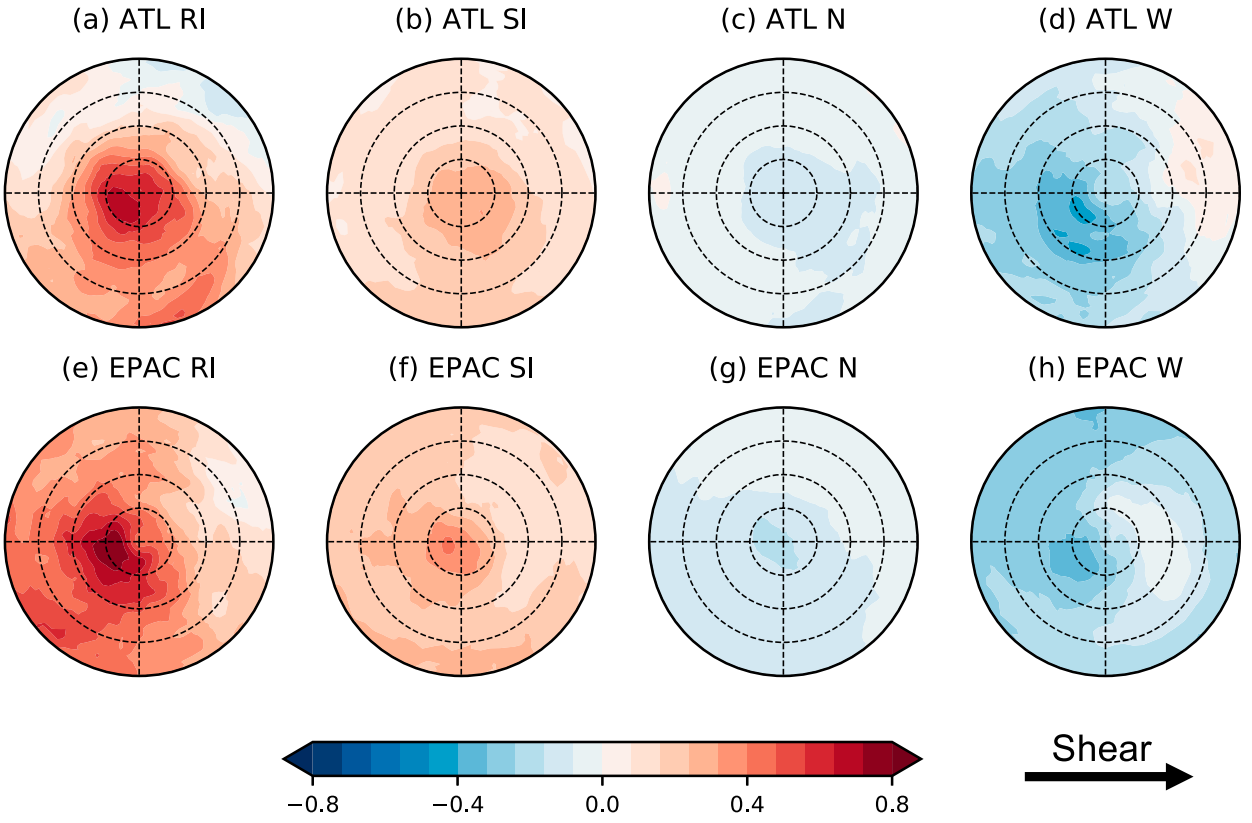

FIG. 8. As in Fig. 3, but for normalized 37-GHz horizontally polarized brightness temperatures. Regions of positive (negative) values are representative of anomalously warm (cold) 37-GHz brightness temperatures.

To quantify the relationship between normalized convective parameters and future TC intensity change, the Pearson correlation coefficient was calculated for area-averaged, upshear, normalized brightness temperatures and future 24-h TC intensity change (Table 5). The area-averaged, innermost 200-km (100 km) normalized IR (microwave) brightness temperatures within the upshear semicircle were used in the calculations. These areas target the spatial locations of greatest differences among intensity change group composites. For each convective parameter tested, large increases in correlation were noted when the normalization technique was employed, demonstrating the potential utility of normalized brightness temperatures in TC intensity prediction. TCs in the eastern North Pacific basin were consistently associated with stronger correlations than TCs in the North Atlantic. This may partially arise from the fact that TC intensity estimates in the eastern North Pacific are more frequently satellite based compared to those in the North Atlantic basin, which has a greater percentage of storms sampled by aircraft reconnaissance (approximately 5% of TC observations in the eastern North Pacific vs about 30% of TC observations in the North Atlantic; Landsea and Franklin 2013). In both basins, out of the three normalized convective parameters, IR brightness temperatures are associated with the strongest correlation to future TC intensity change. Although there is a strong covariance between the IR, 37-GHz, and 85-GHz normalized brightness temperatures, additional information can be acquired when the parameters are combined together, which is discussed further in section 6.

5. Normalized tropical cyclone convective characteristics at RI onset

The previous sections combined all RI episodes into the same RI composite. While this method has the benefit of increasing the sample size of a relatively rare phenomenon, it does not necessarily allow for the analysis of how TC convective evolution is related to RI as an *event*. Prior work has separated the RI episodes that comprise an RI event into those episodes at the onset of the RI event, hereafter referred to as RI onset episodes, and those episodes where RI has already been occurring for at least 12 h, termed RI continuing episodes (Zagrodnik and Jiang 2014; Tao and Jiang 2015; Tao et al. 2017). Such a distinction has revealed prominent differences in the

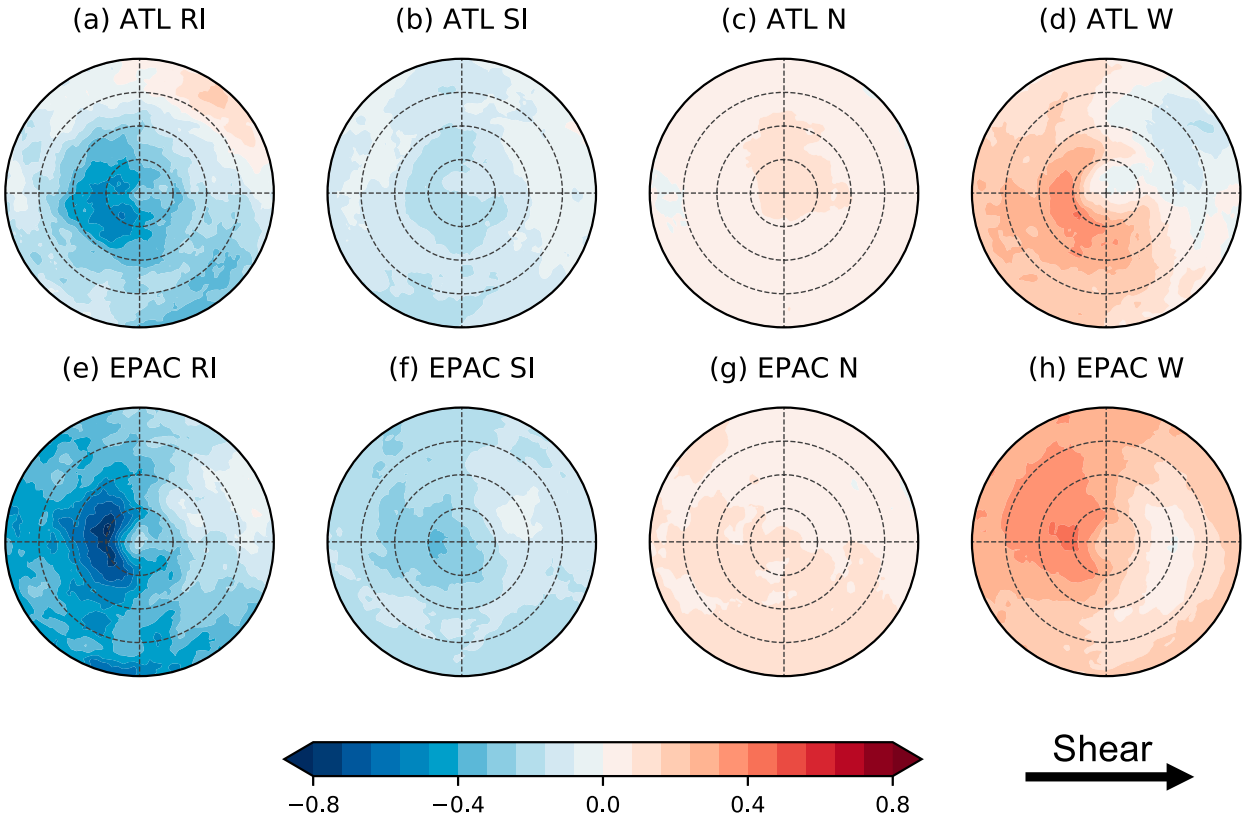

FIG. 9. As in Fig. 3, but for normalized 85-GHz polarization-corrected brightness temperatures. Regions of positive (negative) values are representative of anomalously warm (cold) 85-GHz brightness temperatures.

convective structure of RI episodes near the onset of the event from those episodes where RI has already been ongoing. This section will investigate RI events further, using the normalization technique to account for potential differences in TC intensity between RI onset and RI continuing episodes.

Normalized IR brightness temperature composites of RI events, divided into RI onset and continuing episodes, are shown in Fig. 10. For reference, the composite, normalized, IR brightness temperatures of SI episodes from TCs that do not undergo RI in their lifetime, referred to as null RI events, are also shown to assess whether TCs that undergo RI are associated with unique convective characteristics at the onset of RI. The number of available satellite observations used in the composites of RI onset, RI continuing, and null RI episodes is given in Table 6. Consistent with previous findings, RI continuing episodes in the North Atlantic basin are associated with statistically significantly more negative normalized IR brightness temperatures within the upshear 200 km than RI onset episodes (Figs. 10a,b); however, in the eastern North Pacific basin, similar anomalous upshear IR brightness temperatures are observed in both groups. In both basins, comparing RI onset episodes to null RI episodes reveals that the onset of an RI event is associated with more negative normalized IR brightness temperatures in the upshear quadrants than null RI episodes (Figs. 10a,c and 10d,f). Indeed, differences in the area-averaged, upshear, 200-km normalized IR brightness temperatures between RI onset and null RI episodes are statistically significant.

TABLE 5. Pearson correlation coefficient of raw and normalized area-averaged convective parameters and future 24-h TC intensity change for the North Atlantic (ATL) and eastern North Pacific (EPAC) basins. Area-averaged IR brightness temperatures were calculated in the innermost 200 km of the upshear semicircle and microwave brightness temperatures in the innermost 100 km of the upshear semicircle.

Basin	Raw IR	Raw 37 GHz	Raw 85 GHz	Normalized IR	Normalized 37 GHz	Normalized 85 GHz
ATL	−0.12	0.03	−0.09	−0.35	0.30	−0.31
EPAC	−0.27	0.06	−0.16	−0.49	0.37	−0.43

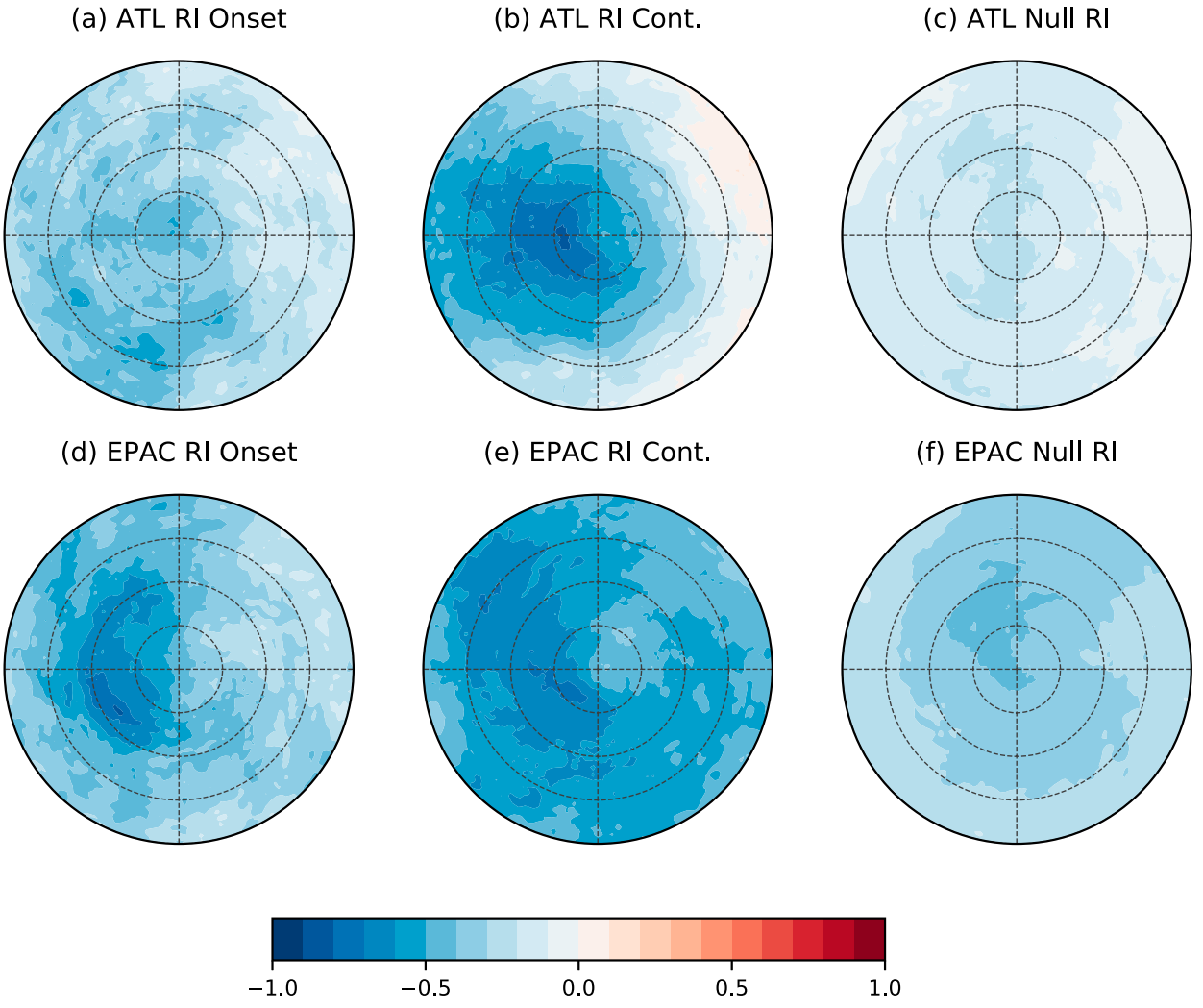

FIG. 10. Composite-mean, storm-centered, shear-relative, normalized infrared brightness temperatures for (a) RI onset, (b) RI continuing, and (c) null RI episodes in the North Atlantic basin. Composites are shown at the beginning of the 24-h intensity change period. Each composite is rotated by the deep-layer (1000–250 hPa) environmental vertical wind shear direction, with the shear vector pointing to the right side of each panel. Dashed radial rings are spaced in 100-km increments. (d)–(f) As in (a)–(c), but for TCs in the eastern North Pacific basin.

RI continuing, RI onset, and null RI episodes were also composited using normalized 37-GHz microwave imagery (Fig. 11). RI continuing episodes (Figs. 11b,e) are associated with the most positive normalized anomalies, and null RI episodes (Figs. 11c,f) are associated with the weakest anomalies of the three groups. As in Fig. 10, the differences between the groups are most pronounced in the upshear regions, indicating the importance of anomalous upshear convection for RI. The differences in the area-averaged normalized 37-GHz brightness temperatures within 75 km in the upshear semicircle, where differences are most pronounced between RI onset and null RI episodes, are statistically significant. Interestingly, the differences between RI continuing and RI onset episodes in this same region are not statistically significant in both basins, despite an increase in the composite normalized 37-GHz brightness temperatures (Figs. 11a,b,d,e). The lack of significant differences of 37-GHz brightness temperatures in RI onset and RI continuing episodes suggests that an increase in anomalous liquid hydrometeor content may not be necessary for the continuation of an RI event.

The pattern of normalized 85-GHz PCT (Fig. 12) resembles that observed from normalized IR brightness temperatures. In the North Atlantic basin, RI continuing episodes are associated with the most negative normalized anomalies (Fig. 12b), while the anomalies in the RI onset composite are notably weaker (Fig. 12a). In the eastern North Pacific, both RI continuing and RI onset episodes are associated with large negative anomalies

TABLE 6. Number of intensity change episodes with available infrared (IR) and passive microwave (MW) imagery for the North Atlantic (ATL) and eastern North Pacific (EPAC) basins.

Intensity change group	ATL IR	ATL MW	EPAC IR	EPAC MW
RI continuing	155	92	216	101
RI onset	106	62	114	55
Null RI	603	329	1007	492

upshear of the TC, which are not significantly different from one another (Figs. 12d,e). In both basins, the null RI composite displays only weak negative normalized anomalies (Figs. 12c,f). Differences in the normalized 85-GHz PCT between RI onset and null RI episodes in the North Atlantic were not significant, indicating the presence of anomalously large frozen hydrometeor content, as represented by ice scattering in the 85-GHz channel, is not necessarily a good predictor of RI onset for TCs in the North Atlantic basin. A significant decrease in normalized 85-GHz brightness temperatures is noted, however, in the RI continuing composite (Fig. 12b), suggesting that anomalously large frozen hydrometeor content may originate as a result of RI rather than act as the trigger of RI, consistent with the findings of Zagrodnik and Jiang (2014), Tao and Jiang (2015), and Tao et al. (2017).

To analyze the evolution of anomalous convective activity relative to the onset of RI, Hovmöller diagrams of

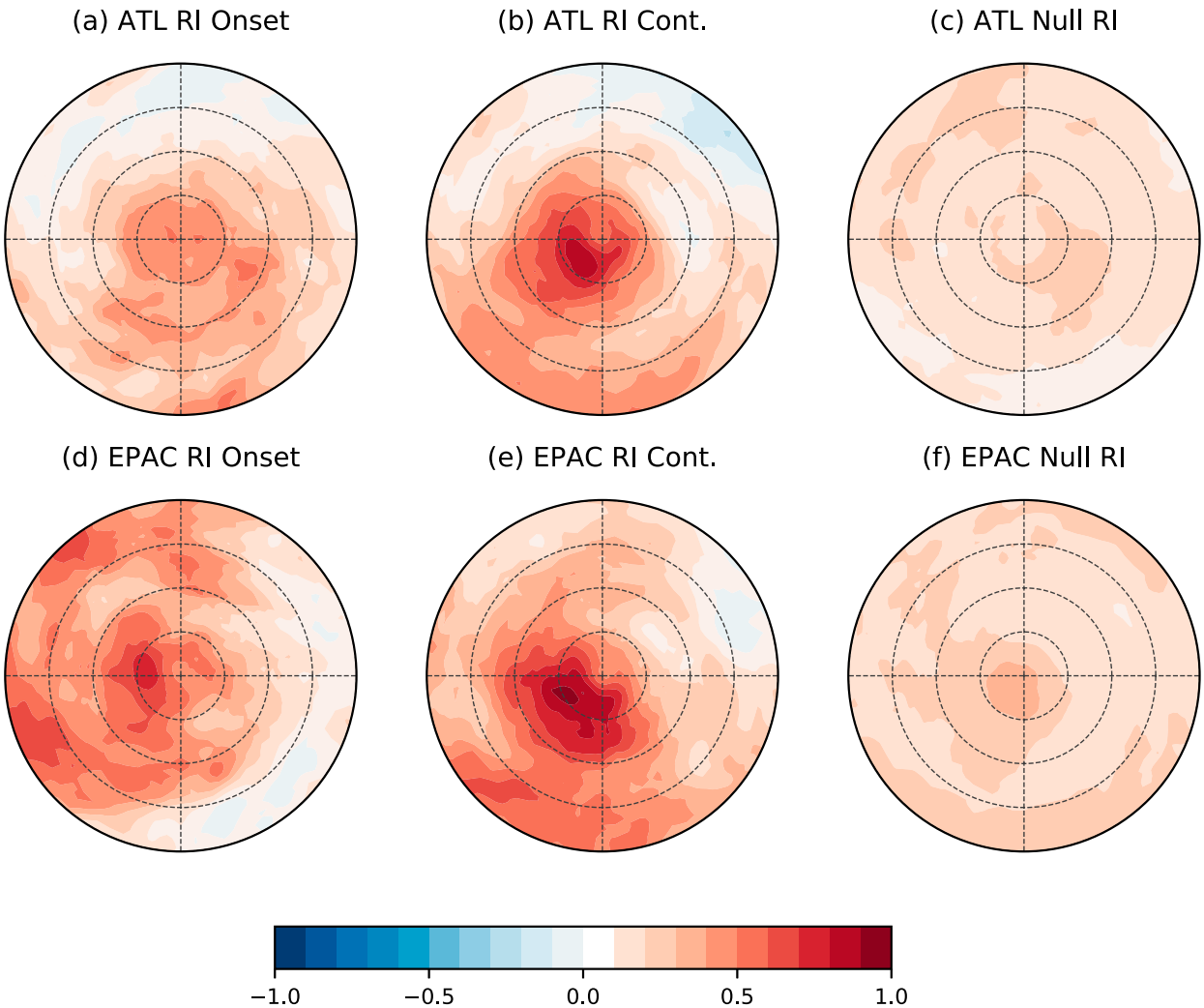

FIG. 11. As in Fig. 10, but for normalized 37-GHz horizontally polarized brightness temperatures. Dashed radial rings are spaced in 50-km increments.

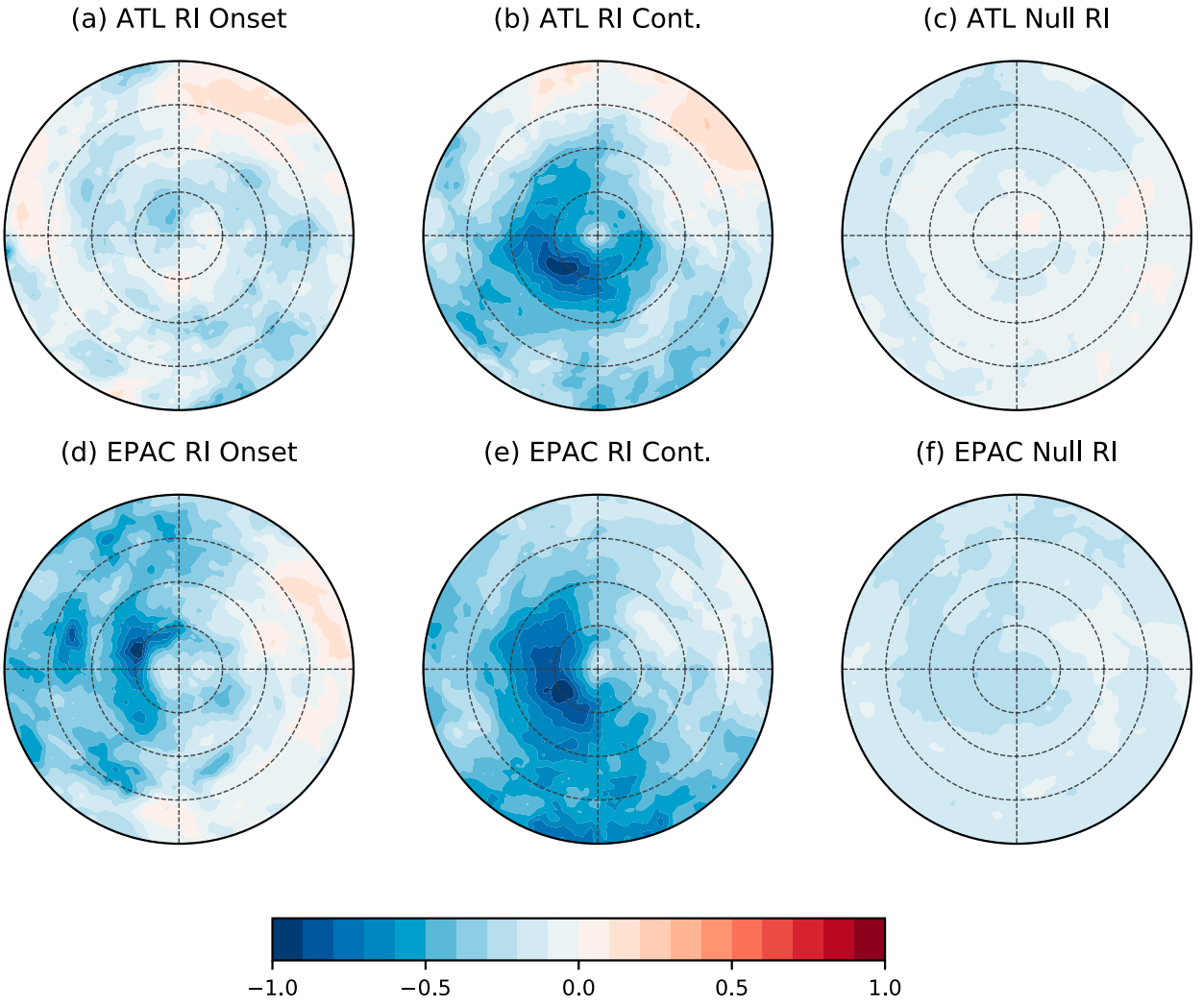

FIG. 12. As in Fig. 11, but for normalized 85-GHz polarization-corrected brightness temperatures.

the three normalized frequencies are shown in Fig. 13. In the North Atlantic basin, normalized IR brightness temperatures are most negative 0–18 h after the onset of RI throughout the innermost 150 km (Fig. 13a). Nonetheless, there is not a sharp increase or decrease in the normalized IR brightness temperatures at any time. Azimuthally averaged, normalized 37-GHz brightness temperatures are most positive approximately 6 h after the onset of RI (Fig. 13b). A sharper increase in the azimuthally averaged, normalized, 37-GHz brightness temperatures, indicative of an increase in anomalous liquid hydrometeor content, is noted between 6 h prior to the onset of RI and 6 h after the onset of RI within the inner 50–100 km, where composite normalized values increase by 0.2–0.3. The evolution of 37-GHz normalized brightness temperatures differs from that of the normalized 85-GHz values (Fig. 13c). The time of the most negative normalized 85-GHz brightness temperatures appears 18 h after the onset of RI, 12 h after the peak in 37-GHz values. Additionally, no notable decreases in the normalized 85-GHz brightness temperatures are observed until after the onset of RI. Since an increase in enhanced liquid water path in 37-GHz imagery around the onset of RI precedes robust ice scattering in 85-GHz imagery, the effects of convection consisting of liquid hydrometeors appears more important for the initiation of RI for TCs in the North Atlantic basin. Thereafter, deep convection that results in robust ice hydrometeor content acts to either help maintain RI or is a consequence of RI.

The evolution of the three normalized convective parameters in the eastern North Pacific basin differs slightly from that of the North Atlantic (Figs. 13d–f). Each of the normalized convective parameters generally has the greatest anomalies 0–12 h after the onset of RI. Notable increases in anomalous ice hydrometeor content are observed in the normalized 85-GHz brightness

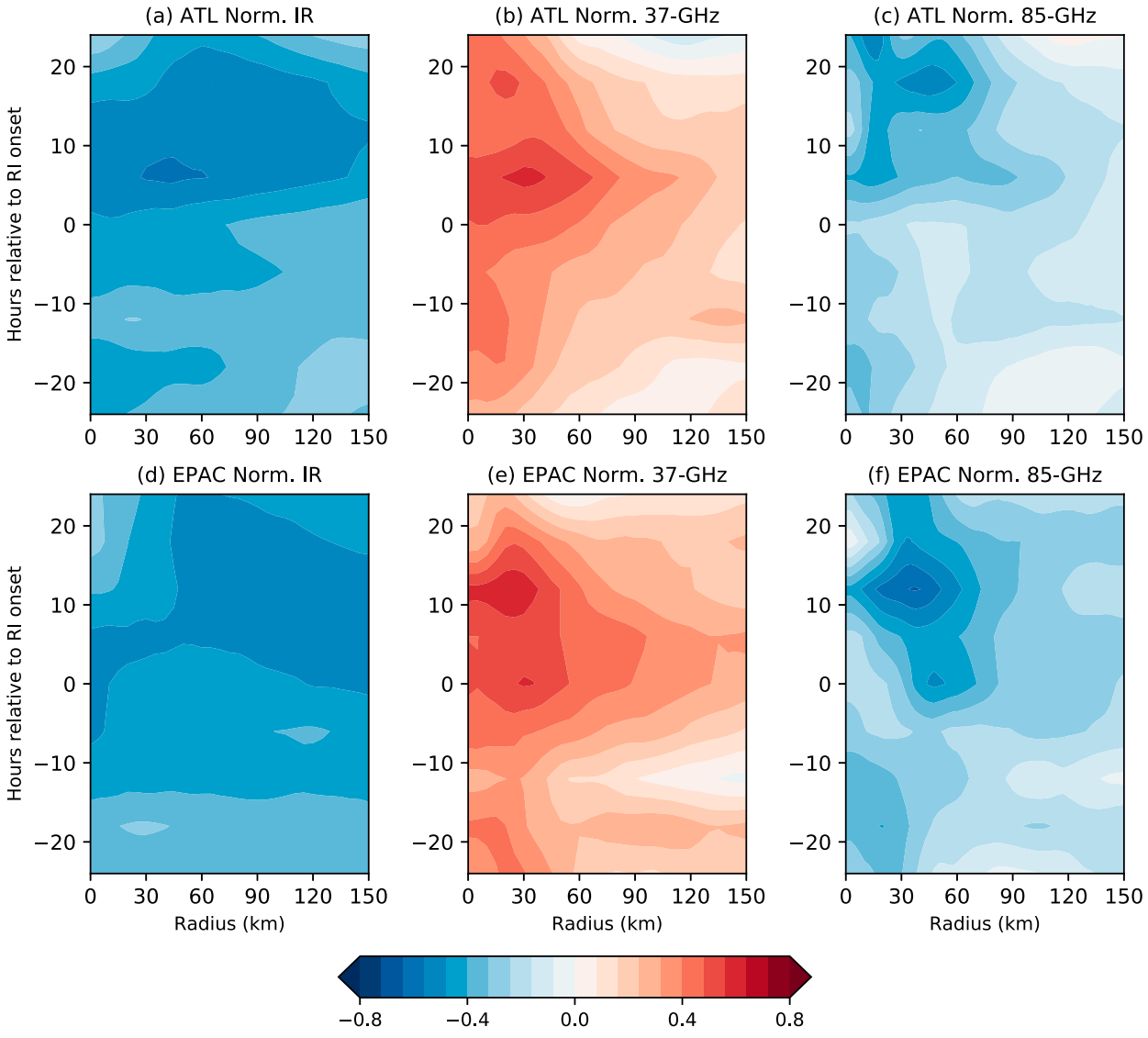

FIG. 13. Composite-mean, azimuthally averaged, normalized (a) infrared brightness temperatures, (b) 37-GHz horizontally polarized brightness temperatures, and (c) 85-GHz polarization-corrected brightness temperatures for RI events in the North Atlantic basin. The time (h) relative to RI onset is plotted along the ordinate, while the radial distance from the TC center (km) is plotted along the abscissa. (d)–(f) As in (a)–(c), but for RI events in the eastern North Pacific basin.

temperatures just before the onset of RI (Fig. 13f). Since the period of peak anomalous convective activity in both normalized 37- and 85-GHz brightness temperatures occur at similar times, it is not clear if convection associated with either anomalous liquid or ice hydrometeor content is more important for the initiation of RI for TCs in the eastern North Pacific basin.

6. Using normalized convective parameters to predict RI

Because of the relatively strong correlation between normalized brightness temperatures and future TC intensity change (Table 5), normalized brightness temperatures were tested as a predictor of all RI episodes, regardless of when they occurred within an RI event. The accuracy of deterministic RI forecasts were verified using the probability of detection (POD) and the false alarm ratio (FAR), as in Harnos and Nesbitt (2016a), as well as the Peirce skill score (PSS; Wilks 2011), similar to Kaplan et al. (2015) and Rozoff et al. (2015). To summarize, the POD is the ratio of the number of correct RI forecasts to the total number of RI episodes. The FAR is the ratio of the number of incorrectly forecast RI episodes (false positives) to the total number of forecast RI episodes. The PSS provides a measure of forecast skill of contingency-type forecasts and is particularly

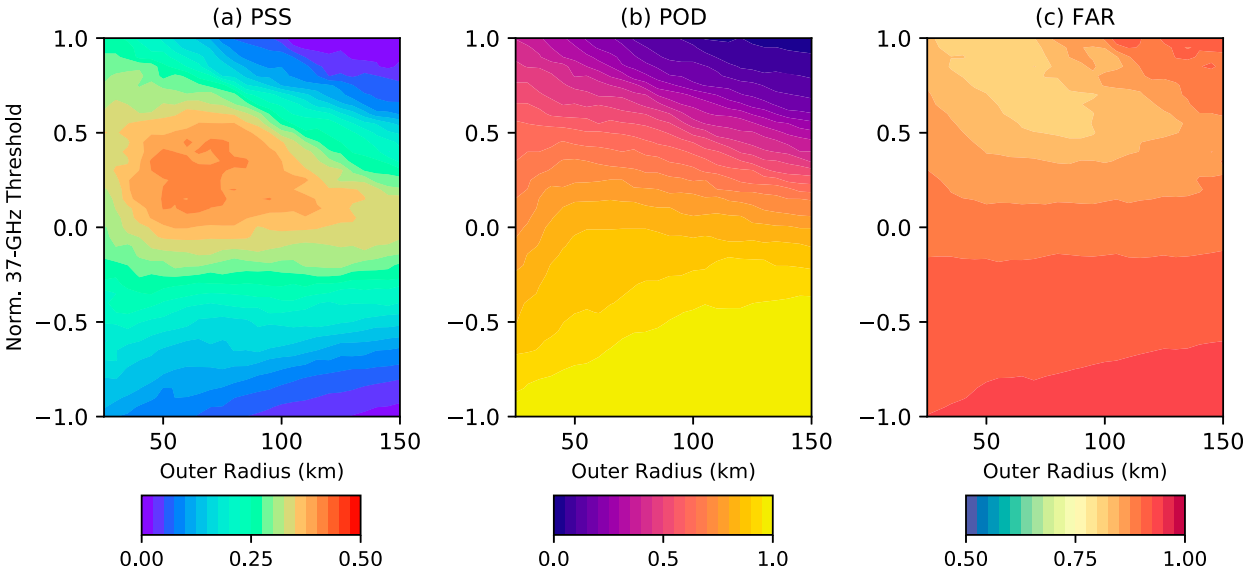

FIG. 14. (a) PSS, (b) POD, and (c) FAR of RI episodes in the North Atlantic basin as functions of the normalized convective threshold and the outer radius used in the area-averaging of normalized brightness temperatures for deterministic forecasts. Normalized 37-GHz brightness temperatures are calculated as the area-averaged values at the onset of the intensity change episode for all radii within the specified outer radius plotted along the abscissa. An RI episode was forecast if the area-averaged, normalized 37-GHz brightness temperatures were greater than the threshold specified along the ordinate.

useful for the evaluation of infrequent events, such as RI (Wilks 2011; Kaplan et al. 2015), and is defined as

$$\mathrm{PSS} = \frac{ad - bc}{(a + c) \times (b + d)}, \tag{2}$$

where a is the number of correctly predicted RI episodes, b is the number of predicted RI episodes that did not verify, c is the number of predicted non-RI episodes that did not verify, and d is the number of correctly predicted non-RI episodes. The PSS is bounded by values of -1 and 1, where a perfect forecast yields of a value of 1, while negative values indicate unskillful forecasts.

Since area averages of normalized brightness temperatures near the TC center tend to have a stronger relationship to future TC intensity change than point-based brightness temperature predictors (not shown), the relationship between RI and various area-averaged normalized convective parameters were tested. When calculating the skill of the area-averaged normalized brightness temperature as a predictor of RI, both azimuthally averaged quantities, as well as area-averaged shear-relative quadrants, were tested. It was determined that azimuthally averaged quantities resulted in the greatest forecast skill. To determine which convective regions yielded the most skill, the PSS, POD, and FAR were calculated as a function of the averaging radius. The deterministic RI forecasts tested here also require a threshold of area-averaged, normalized brightness temperatures to predict whether an RI episode will or will not occur. In other words, when area-averaged, normalized brightness temperatures featured anomalously greater convective activity than a given threshold, an RI episode was forecasted to occur. To determine the normalized brightness temperature threshold that results in the greatest forecast skill, hindcast deterministic RI forecasts were issued as a function of both the radius used in the area-averaged, normalized brightness temperature calculations, as well as the normalized brightness temperature threshold, using brightness temperatures at the onset of the intensity change episode.

An example of the results of this process for TCs in the North Atlantic basin is shown in Fig. 14. In this example, RI was forecasted to occur if the area-averaged, normalized 37-GHz brightness temperatures exceeded the specified threshold along the ordinate. Forecasts of RI using the area-averaged, normalized 37-GHz brightness temperatures yielded the highest PSS when a threshold between approximately 0–0.5 was used in conjunction with brightness temperatures averaged between approximately 0–50 km and 0–80 km (Fig. 14a). For thresholds larger than 0.5, the FAR decreases, especially at smaller radii, but the POD also decreases rapidly. Below the threshold of 0, the POD increases, but the FAR also increases (Figs. 14b,c). The "Goldilocks zone" of maximum PSS, seen in Fig. 14a, yields the best combination of outer radius and normalized brightness

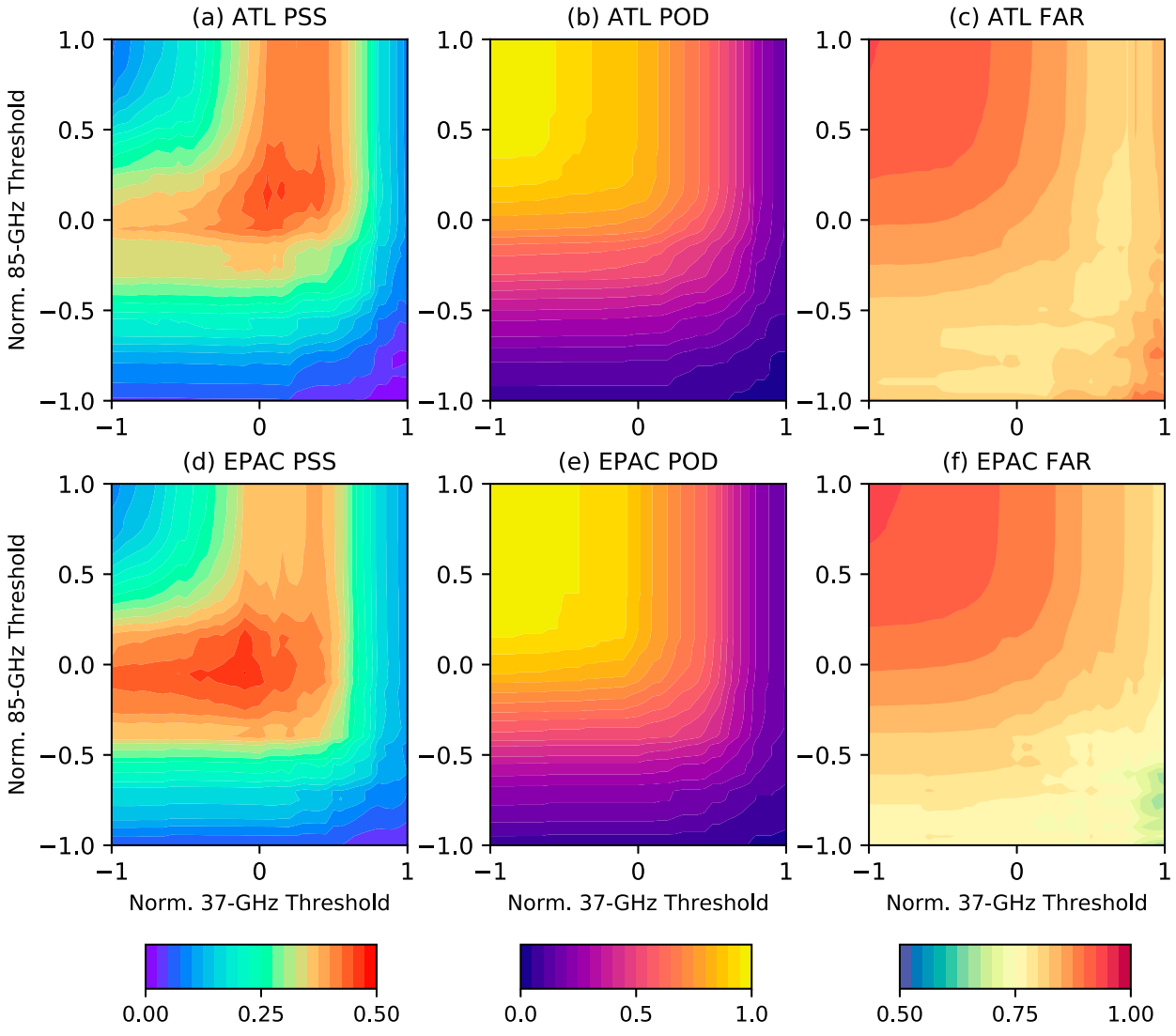

FIG. 15. (a) PSS, (b) POD, and (c) FAR of RI episodes in the North Atlantic basin as a function of the normalized convective threshold used in deterministic forecasts. Normalized 37-GHz brightness temperatures are calculated as the area-averaged values for all radii within 75 km from the TC center and 85-GHz brightness temperatures for all radii within 100 km of the TC center. Both the normalized 37-GHz and 85-GHz brightness temperatures are calculated at the onset of the intensity change episode. An RI episode was forecast if the area-averaged, normalized 85-GHz brightness temperatures were less than the threshold specified along the ordinate and the area-averaged, normalized 37-GHz brightness temperatures were greater than the threshold specified along the abscissa. (d)–(f) As in (a)–(c), but for TCs in the eastern North Pacific basin.

temperature threshold that maximizes the POD and minimizes the FAR. Figure 14 demonstrates that skillful forecasts of RI can be made even if the only information known about a TC is the normalized 37-GHz brightness temperatures at the beginning of the intensity change episode. Deterministic RI forecasts utilizing normalized IR and 85-GHz brightness temperatures also yielded skillful forecasts with comparable PSS, POD, and FAR values to those of normalized 37-GHz brightness temperatures (not shown).

Incorporating multiple normalized convective parameters increased the skill of deterministic RI forecasts. An example of this process is shown in Fig. 15, using both normalized 37- and 85-GHz brightness temperatures. Normalized 37-GHz (85 GHz) brightness temperatures were calculated as the area-averaged values within the innermost 75 (100) km of the TC, which were determined to be the regions that yielded maximum forecast skill. As seen in Fig. 15a, maximum PSS values have increased from those observed in Fig. 14a, to approximately 0.46, for RI predictions in the

North Atlantic basin. This value is larger than the maximum PSS that results from using any threshold of normalized 37- or 85-GHz brightness temperatures alone. The skill of RI forecasts in the eastern North Pacific basin using the same normalized convective parameters is even greater, with maximum PSS values of approximately 0.48 (Fig. 15d). Although these values indicate skillful forecasts, it should be noted that nearly the entire parameter space is characterized by FAR values >0.75 (Figs. 15c and 15f), which is undesirably high, but comparable to current operational model predictions of RI (Kaplan et al. 2015; Rozoff et al. 2015).

Although the methods used to predict RI episodes in this section are by no means complete, they are intended to demonstrate normalized brightness temperatures can act as skillful predictors of RI. Incorporating environmental predictors has been shown to further improve the skill of RI forecasts (Kaplan et al. 2015; Rozoff et al. 2015). It should be mentioned that the predictive results shown in this study are developmental; thus, the outcomes might differ for either an independent sample or in an operational environment. Using normalized brightness temperatures to predict RI episodes would also benefit from the development of a probabilistic predictive algorithm rather than the deterministic threshold approach described here.

7. Conclusions

This study introduces a novel convective normalization technique to analyze the relationship between TC convective characteristics, as determined from IR and passive microwave brightness temperatures, and future TC intensity change. The convective normalization technique diagnoses the anomalous convective activity associated with TCs by accounting for how convection varies as a function of TC intensity, effectively removing potential intensity-driven biases, such as depressed microwave brightness temperatures driven by ice hydrometeor advection or enhanced microwave brightness temperatures caused by a disturbed sea state (Harnos and Nesbitt 2016a). Both the observed and normalized convective structures of TCs in the North Atlantic and eastern North Pacific basins were assessed through composite analyses. Composites of four TC intensity change groups [rapid intensification (RI), slow intensification (SI), neutral (N), and weakening (W)] were analyzed in a shear-relative framework.

The composite analysis of observed IR and passive microwave brightness temperatures indicate that increased convective activity in the upshear quadrants of the TC is associated with increased rates of TC intensification, with the exception of W episodes, which are composed of the most intense TCs on average. The differences in intensity distributions between the intensity change groups was accounted for by normalizing the IR and passive microwave brightness temperatures, which displayed a clear progression of anomalously symmetric and enhanced convection being associated with the greatest rates of TC intensification to anomalously asymmetric and weak convection being associated with weakening TCs. These findings are consistent with previous climatological analyses of TC convective characteristics that utilize remote sensing observations (Harnos and Nesbitt 2011; Zagrodnik and Jiang 2014; Alvey et al. 2015; Tao and Jiang 2015; Harnos and Nesbitt 2016a; Shimada et al. 2017; Tao et al. 2017) as well as previous studies that highlight the efficiency of symmetric convection for TC intensification (Nolan and Grasso 2003; Nolan et al. 2007). In particular, the most anomalous convection in RI episodes was observed in the upshear quadrants of the TC core, which is a region prior studies have shown to be important for increased rates of TC intensification (Stevenson et al. 2014; Fischer et al. 2017; Rios-Berrios and Torn 2017). The area-averaged, normalized IR, 37-GHz, and 85-GHz brightness temperatures within the TC core had much larger correlation coefficients with future TC intensity change compared to using the raw brightness temperatures.

The role of the evolution of anomalous convection in RI was also assessed by separating RI episodes into two groups. The first group, referred to as RI onset episodes, was composed of the first RI episode observed in any RI event. The second group, referred to as RI continuing episodes, was defined as those RI episodes where RI had already been occurring for at least 12 h. In the North Atlantic, RI continuing episodes were associated with anomalous IR and 85-GHz brightness temperatures that were significantly colder than RI onset events, consistent with Zagrodnik and Jiang (2014), Tao and Jiang (2015), and Tao et al. (2017). RI onset episodes tended to have significantly greater anomalous convective activity than null RI episodes, with the exception of normalized 85-GHz PCT in the North Atlantic, where the RI onset composite was similar to the null RI composite, suggesting convection containing anomalously large ice hydrometeor content is not necessary for the onset of RI. Hovmöller diagrams of normalized brightness temperatures as a function of time relative to the onset of RI showed anomalously large liquid hydrometeor content, as determined by an increase in the normalized 37-GHz brightness temperatures, preceded an increase in anomalous ice hydrometeors, as determined by a decrease in the normalized 85-GHz brightness temperatures, consistent with Tao and Jiang (2015) and Tao et al. (2017) who argue deep convection does not trigger an RI event, but

instead originates as a result of RI. It has also been hypothesized that TC intensification, including RI, is strongly tied to boundary layer dynamics. Thus, the relationship of deep convection, if necessary at all, to trigger unbalanced processes within the boundary layer that can lead to RI, requires further understanding (Wissmeier and Smith 2011; Montgomery and Smith 2014; Smith and Montgomery 2016). On the other hand, it is possible that, in some cases, the relatively short time scale of deep convective bursts, and their associated ice-scattering signatures, went undetected by the microwave satellite observing network because of its irregular sampling rate and relatively poor temporal resolution for any given TC.

It should be noted that the convective evolution of RI events in the eastern North Pacific basin was associated with different normalized convective characteristics compared to the North Atlantic basin. In particular, for all three normalized convective parameters, differences between RI continuing and RI onset episodes were insignificant in regions near the TC center. Additionally, RI onset episodes in the eastern North Pacific were associated with significantly more negative normalized 85-GHz brightness temperatures than null RI episodes. The differences between basins raise the question if basin-dependent RI pathways exist, possibly because of differences in TC environments, such as vertical wind shear. Even within the same basin, simulations of two separate RI events in the North Atlantic by Harnos and Nesbitt (2016b, c) indicate that the magnitude of the vertical wind shear is closely related to the symmetry and intensity of convection around the time of RI, consistent with the observational study performed by Harnos and Nesbitt (2011), which demonstrated greater wind shear magnitudes favor a greater probability for deep convection.

Because of the association between normalized brightness temperatures and RI, normalized IR and passive microwave brightness temperatures were tested as predictors of RI. Normalized brightness temperatures can skillfully predict episodes of RI with only knowledge of the convective structure of a TC at the onset of the intensity change episode. Predictions of RI episodes using normalized brightness temperatures yielded comparable skill to operational statistical models of RI prediction.

Future work would benefit from developing more complex statistical models of RI prediction that include normalized IR and passive microwave brightness temperatures, environmental conditions (e.g., vertical wind shear, potential intensity, moisture), and the kinematic structure of the TC (e.g., the spatial pattern of normalized brightness temperatures relative to the radius of maximum wind). Additional future work plans to assess whether normalized brightness temperatures can be used to skillfully predict the onset and cessation of RI events on independent TC samples.

A better understanding of the convective processes affecting RI is vital for improving TC intensity forecasts. With the recent launch of the *Geostationary Operational Environmental Satellite 16* (*GOES-16*), a higher spatial and temporal resolution IR dataset will soon be available to further analyze how observed and normalized brightness temperatures are related to TC intensity change and RI.

Acknowledgments. The authors thank the helpful comments of Dr. Steve Nesbitt and two anonymous reviewers, which helped to improve the clarity and quality of this analysis. This work was funded by NASA Grant NNX17AG95G.

REFERENCES

Alvey, G. R., III, J. Zawislak, and E. Zipser, 2015: Precipitation properties observed during tropical cyclone intensity change. *Mon. Wea. Rev.*, **143**, 4476–4492, https://doi.org/10.1175/MWR-D-15-0065.1.

Bister, M., and K. A. Emanuel, 2002: Low frequency variability of tropical cyclone potential intensity 1. Interannual to interdecadal variability. *J. Geophys. Res.*, **107**, 4801, https://doi.org/10.1029/2001JD000776.

Cecil, D. J., and E. J. Zipser, 1999: Relationships between tropical cyclone intensity and satellite-based indicators of inner core convection: 85-GHz ice-scattering signature and lightning. *Mon. Wea. Rev.*, **127**, 103–123, https://doi.org/10.1175/1520-0493(1999)127<0103:RBTCIA>2.0.CO;2.

Chen, H., and D.-L. Zhang, 2013: On the rapid intensification of Hurricane Wilma (2005). Part II: Convective bursts and the upper-level warm core. *J. Atmos. Sci.*, **70**, 146–162, https://doi.org/10.1175/JAS-D-12-062.1.

Chen, S. S., J. A. Knaff, and F. D. Marks, 2006: Effects of vertical wind shear and storm motion on tropical cyclone rainfall asymmetries deduced from TRMM. *Mon. Wea. Rev.*, **134**, 3190–3208, https://doi.org/10.1175/MWR3245.1.

Corbosiero, K. L., and J. Molinari, 2002: The effects of vertical wind shear on the distribution of convection in tropical cyclones. *Mon. Wea. Rev.*, **130**, 2110–2123, https://doi.org/10.1175/1520-0493(2002)130<2110:TEOVWS>2.0.CO;2.

——, and ——, 2003: The relationship between storm motion, vertical wind shear, and convective asymmetries in tropical cyclones. *J. Atmos. Sci.*, **60**, 366–376, https://doi.org/10.1175/1520-0469(2003)060<0366:TRBSMV>2.0.CO;2.

Davis, C., C. Snyder, and A. C. Didlake, 2008: A vortex-based perspective of eastern Pacific tropical cyclone formation. *Mon. Wea. Rev.*, **136**, 2461–2477, https://doi.org/10.1175/2007MWR2317.1.

Dee, D. P., and Coauthors, 2011: The ERA-Interim reanalysis: Configuration and performance of the data assimilation system. *Quart. J. Roy. Meteor. Soc.*, **137**, 553–597, https://doi.org/10.1002/qj.828.

DeHart, J. C., R. A. Houze, and R. F. Rogers, 2014: Quadrant distribution of tropical cyclone inner-core kinematics in relation to environmental shear. *J. Atmos. Sci.*, **71**, 2713–2732, https://doi.org/10.1175/JAS-D-13-0298.1.

DeMaria, M., C. R. Sampson, J. A. Knaff, and K. D. Musgrave, 2014: Is tropical cyclone intensity guidance improving? *Bull. Amer. Meteor. Soc.*, **95**, 387–398, https://doi.org/10.1175/BAMS-D-12-00240.1.

Dvorak, V. F., 1975: Tropical cyclone intensity analysis and forecasting from satellite imagery. *Mon. Wea. Rev.*, **103**, 420–430, https://doi.org/10.1175/1520-0493(1975)103<0420:TCIAAF>2.0.CO;2.

Emanuel, K., and F. Zhang, 2016: On the predictability and error sources of tropical cyclone intensity forecasts. *J. Atmos. Sci.*, **73**, 3739–3747, https://doi.org/10.1175/JAS-D-16-0100.1.

Fischer, M. S., B. H. Tang, and K. L. Corbosiero, 2017: Assessing the influence of upper-tropospheric troughs on tropical cyclone intensification rates after genesis. *Mon. Wea. Rev.*, **145**, 1295–1313, https://doi.org/10.1175/MWR-D-16-0275.1.

Guimond, S. R., G. M. Heymsfield, and F. J. Turk, 2010: Multiscale observations of Hurricane Dennis (2005): The effects of hot towers on rapid intensification. *J. Atmos. Sci.*, **67**, 633–654, https://doi.org/10.1175/2009JAS3119.1.

——, ——, P. D. Reasor, and A. C. Didlake, 2016: The rapid intensification of Hurricane Karl (2010): New remote sensing observations of convective bursts from the Global Hawk platform. *J. Atmos. Sci.*, **73**, 3617–3639, https://doi.org/10.1175/JAS-D-16-0026.1.

Hack, J. J., and W. H. Schubert, 1986: Nonlinear response of atmospheric vortices to heating by organized cumulus convection. *J. Atmos. Sci.*, **43**, 1559–1573, https://doi.org/10.1175/1520-0469(1986)043<1559:NROAVT>2.0.CO;2.

Harnos, D. S., and S. W. Nesbitt, 2011: Convective structure in rapidly intensifying tropical cyclones as depicted by passive microwave measurements. *Geophys. Res. Lett.*, **38**, L07805, https://doi.org/10.1029/2011GL047010.

——, and ——, 2016a: Passive microwave quantification of tropical cyclone inner-core cloud populations relative to subsequent intensity change. *Mon. Wea. Rev.*, **144**, 4461–4482, https://doi.org/10.1175/MWR-D-15-0090.1.

——, and ——, 2016b: Varied pathways for simulated tropical cyclone rapid intensification. Part I: Precipitation and environment. *Quart. J. Roy. Meteor. Soc.*, **142**, 1816–1831, https://doi.org/10.1002/qj.2780.

——, and ——, 2016c: Varied pathways for simulated tropical cyclone rapid intensification. Part II: Vertical motion and cloud populations. *Quart. J. Roy. Meteor. Soc.*, **142**, 1832–1846, https://doi.org/10.1002/qj.2778.

Hart, R. E., and J. L. Evans, 2001: A climatology of the extratropical transition of Atlantic tropical cyclones. *J. Climate*, **14**, 546–564, https://doi.org/10.1175/1520-0442(2001)014<0546:ACOTET>2.0.CO;2.

Hawkins, J. D., F. J. Turk, T. F. Lee, and K. Richardson, 2008: Observations of tropical cyclones with the SSMIS. *IEEE Trans. Geosci. Remote Sens.*, **46**, 901–912, https://doi.org/10.1109/TGRS.2008.915753.

Hendricks, E. A., M. S. Peng, B. Fu, and T. Li, 2010: Quantifying environmental control on tropical cyclone intensity change. *Mon. Wea. Rev.*, **138**, 3243–3271, https://doi.org/10.1175/2010MWR3185.1.

Jones, T. A., and D. J. Cecil, 2006: Histogram matching of ASMR-E and TMI brightness temperatures. Preprints, *14th Conf. on Satellite Meteorology and Oceanography*, Atlanta, GA, Amer. Meteor. Soc., P1.23, https://ams.confex.com/ams/Annual2006/techprogram/paper_100880.htm.

Kaplan, J., and M. DeMaria, 2003: Large-scale characteristics of rapidly intensifying tropical cyclones in the North Atlantic basin. *Wea. Forecasting*, **18**, 1093–1108, https://doi.org/10.1175/1520-0434(2003)018<1093:LCORIT>2.0.CO;2.

——, ——, and J. A. Knaff, 2010: A revised tropical cyclone rapid intensification index for the Atlantic and eastern North Pacific basins. *Wea. Forecasting*, **25**, 220–241, https://doi.org/10.1175/2009WAF2222280.1.

——, and Coauthors, 2015: Evaluating environmental impacts on tropical cyclone rapid intensification predictability utilizing statistical models. *Wea. Forecasting*, **30**, 1374–1396, https://doi.org/10.1175/WAF-D-15-0032.1.

Kieper, M. E., and H. Jiang, 2012: Predicting tropical cyclone rapid intensification using the 37 GHz ring pattern identified from passive microwave measurements. *Geophys. Res. Lett.*, **39**, L13804, https://doi.org/10.1029/2012GL052115.

Knapp, K. R., and Coauthors, 2011: Globally gridded satellite observations for climate studies. *Bull. Amer. Meteor. Soc.*, **92**, 893–907, https://doi.org/10.1175/2011BAMS3039.1.

Landsea, C. W., and J. L. Franklin, 2013: Atlantic hurricane database uncertainty and presentation of a new database format. *Mon. Wea. Rev.*, **141**, 3576–3592, https://doi.org/10.1175/MWR-D-12-00254.1.

Lee, T. F., F. J. Turk, J. Hawkins, and K. Richardson, 2002: Interpretation of TRMM TMI images of tropical cyclones. *Earth Interact.*, **6**, https://doi.org/10.1175/1087-3562(2002)006<0001:IOTTIO>2.0.CO;2.

Montgomery, M. T., and R. K. Smith, 2014: Paradigms for tropical cyclone intensification. *Aust. Meteor. Oceanogr.*, **64**, 37–66, https://doi.org/10.22499/2.6401.005.

Nolan, D. S., and L. D. Grasso, 2003: Nonhydrostatic, three-dimensional perturbations to balanced, hurricane-like vortices. Part II: Symmetric response and nonlinear simulations. *J. Atmos. Sci.*, **60**, 2717–2745, https://doi.org/10.1175/1520-0469(2003)060<2717:NTPTBH>2.0.CO;2.

——, Y. Moon, and D. P. Stern, 2007: Tropical cyclone intensification from asymmetric convection: Energetics and efficiency. *J. Atmos. Sci.*, **64**, 3377–3405, https://doi.org/10.1175/JAS3988.1.

Pendergrass, A. G., and H. E. Willoughby, 2009: Diabatically induced secondary flows in tropical cyclones. Part I: Quasi-steady forcing. *Mon. Wea. Rev.*, **137**, 805–821, https://doi.org/10.1175/2008MWR2657.1.

Rappaport, E. N., J.-G. Jiing, C. W. Landsea, S. T. Murillo, and J. L. Franklin, 2012: The Joint Hurricane Test Bed: Its first decade of tropical cyclone research-to-operations activities reviewed. *Bull. Amer. Meteor. Soc.*, **93**, 371–380, https://doi.org/10.1175/BAMS-D-11-00037.1.

Rios-Berrios, R., and R. D. Torn, 2017: Climatological analysis of tropical cyclone intensity changes under moderate vertical wind shear. *Mon. Wea. Rev.*, **145**, 1717–1738, https://doi.org/10.1175/MWR-D-16-0350.1.

Rogers, R., P. Reasor, and S. Lorsolo, 2013: Airborne Doppler observations of the inner-core structural differences between intensifying and steady-state tropical cyclones. *Mon. Wea. Rev.*, **141**, 2970–2991, https://doi.org/10.1175/MWR-D-12-00357.1.

——, ——, and J. A. Zhang, 2015: Multiscale structure and evolution of Hurricane Earl (2010) during rapid intensification. *Mon. Wea. Rev.*, **143**, 536–562, https://doi.org/10.1175/MWR-D-14-00175.1.

Rozoff, C. M., and J. P. Kossin, 2011: New probabilistic forecast models for the prediction of tropical cyclone rapid intensification. *Wea. Forecasting*, **26**, 677–689, https://doi.org/10.1175/WAF-D-10-05059.1.

——, C. S. Velden, J. Kaplan, J. P. Kossin, and A. J. Wimmers, 2015: Improvements in the probabilistic prediction of tropical cyclone rapid intensification with passive microwave observations. *Wea. Forecasting*, **30**, 1016–1038, https://doi.org/10.1175/WAF-D-14-00109.1.

Sampson, C. R., J. Kaplan, J. A. Knaff, M. DeMaria, and C. A. Sisko, 2011: A deterministic rapid intensification aid. *Wea. Forecasting*, **26**, 579–585, https://doi.org/10.1175/WAF-D-10-05010.1.

Schubert, W. H., and J. J. Hack, 1982: Inertial stability and tropical cyclone development. *J. Atmos. Sci.*, **39**, 1687–1697, https://doi.org/10.1175/1520-0469(1982)039<1687:ISATCD>2.0.CO;2.

Shapiro, L. J., and H. E. Willoughby, 1982: The response of balanced hurricanes to local sources of heat and momentum. *J. Atmos. Sci.*, **39**, 378–394, https://doi.org/10.1175/1520-0469(1982)039<0378:TROBHT>2.0.CO;2.

Shimada, U., K. Aonashi, and Y. Miyamoto, 2017: Tropical cyclone intensity change and axisymmetricity deduced from GSMaP. *Mon. Wea. Rev.*, **145**, 1003–1017, https://doi.org/10.1175/MWR-D-16-0244.1.

Smith, R. K., and M. T. Montgomery, 2016: The efficiency of diabatic heating and tropical cyclone intensification. *Quart. J. Roy. Meteor. Soc.*, **142**, 2081–2086, https://doi.org/10.1002/qj.2804.

Spencer, R. W., H. M. Goodman, and R. E. Hood, 1989: Precipitation retrieval over land and ocean with the SSM/I: Identification and characteristics of the scattering signal. *J. Atmos. Oceanic Technol.*, **6**, 254–273, https://doi.org/10.1175/1520-0426(1989)006<0254:PROLAO>2.0.CO;2.

Stevenson, S. N., K. L. Corbosiero, and J. Molinari, 2014: The convective evolution and rapid intensification of Hurricane Earl (2010). *Mon. Wea. Rev.*, **142**, 4364–4380, https://doi.org/10.1175/MWR-D-14-00078.1.

——, ——, and S. F. Abarca, 2016: Lightning in eastern North Pacific tropical cyclones: A comparison to the North Atlantic. *Mon. Wea. Rev.*, **144**, 225–239, https://doi.org/10.1175/MWR-D-15-0276.1.

——, ——, M. DeMaria, and J. L. Vigh, 2018: A 10-year survey of tropical cyclone inner-core lightning bursts and their relationship to intensity change. *Wea. Forecasting*, **33**, 23–36, https://doi.org/10.1175/WAF-D-17-0096.1.

Susca-Lopata, G., J. Zawislak, E. J. Zipser, and R. F. Rogers, 2015: The role of observed environmental conditions and precipitation evolution in the rapid intensification of Hurricane Earl (2010). *Mon. Wea. Rev.*, **143**, 2207–2223, https://doi.org/10.1175/MWR-D-14-00283.1.

Tang, B., and K. Emanuel, 2012: A ventilation index for tropical cyclones. *Bull. Amer. Meteor. Soc.*, **93**, 1901–1912, https://doi.org/10.1175/BAMS-D-11-00165.1.

Tao, C., and H. Jiang, 2015: Distributions of shallow to very deep precipitation–convection in rapidly intensifying tropical cyclones. *J. Climate*, **28**, 8791–8824, https://doi.org/10.1175/JCLI-D-14-00448.1.

——, ——, and J. Zawislak, 2017: The relative importance of stratiform and convective rainfall in rapidly intensifying tropical cyclones. *Mon. Wea. Rev.*, **145**, 795–809, https://doi.org/10.1175/MWR-D-16-0316.1.

Torn, R. D., and C. Snyder, 2012: Uncertainty of tropical cyclone best-track information. *Wea. Forecasting*, **27**, 715–729, https://doi.org/10.1175/WAF-D-11-00085.1.

Velden, C., and Coauthors, 2006: The Dvorak tropical cyclone intensity estimation technique: A satellite-based method that has endured for over 30 years. *Bull. Amer. Meteor. Soc.*, **87**, 1195–1210, https://doi.org/10.1175/BAMS-87-9-1195.

——, T. Olander, D. Herndon, and J. P. Kossin, 2017: Reprocessing the most intense historical tropical cyclones in the satellite era using the advanced Dvorak technique. *Mon. Wea. Rev.*, **145**, 971–983, https://doi.org/10.1175/MWR-D-16-0312.1.

Vigh, J. L., and W. H. Schubert, 2009: Rapid development of the tropical cyclone warm core. *J. Atmos. Sci.*, **66**, 3335–3350, https://doi.org/10.1175/2009JAS3092.1.

Vivekanandan, J., J. Turk, and V. N. Bringi, 1991: Ice water path estimation and characterization using passive microwave radiometry. *J. Appl. Meteor.*, **30**, 1407–1421, https://doi.org/10.1175/1520-0450(1991)030<1407:IWPEAC>2.0.CO;2.

Wang, H., and Y. Wang, 2014: A numerical study of Typhoon Megi (2010). Part I: Rapid intensification. *Mon. Wea. Rev.*, **142**, 29–48, https://doi.org/10.1175/MWR-D-13-00070.1.

Wilheit, T. T., 1986: Some comments on passive microwave measurement of rain. *Bull. Amer. Meteor. Soc.*, **67**, 1226–1232, https://doi.org/10.1175/1520-0477(1986)067<1226:SCOPMM>2.0.CO;2.

Wilks, D., 2011: *Statistical Methods in the Atmospheric Sciences*. Elsevier, 704 pp.

Wimmers, A. J., and C. S. Velden, 2010: Objectively determining the rotational center of tropical cyclones in passive microwave satellite imagery. *J. Appl. Meteor. Climatol.*, **49**, 2013–2034, https://doi.org/10.1175/2010JAMC2490.1.

Wissmeier, U., and R. K. Smith, 2011: Tropical cyclone convection: The effects of ambient vertical vorticity. *Quart. J. Roy. Meteor. Soc.*, **137**, 845–857, https://doi.org/10.1002/qj.819.

Wu, R., and J. A. Weinman, 1984: Microwave radiances from precipitating clouds containing aspherical ice, combined phase, and liquid hydrometeors. *J. Geophys. Res.*, **89**, 7170–7178, https://doi.org/10.1029/JD089iD05p07170.

Zagrodnik, J. P., and H. Jiang, 2014: Rainfall, convection, and latent heating distributions in rapidly intensifying tropical cyclones. *J. Atmos. Sci.*, **71**, 2789–2809, https://doi.org/10.1175/JAS-D-13-0314.1.

Zhang, D.-L., and H. Chen, 2012: Importance of the upper-level warm core in the rapid intensification of a tropical cyclone. *Geophys. Res. Lett.*, **39**, L02806, https://doi.org/10.1029/2011GL050578.